Lysosomal dysfunction in Down Syndrome and Alzheimer mouse models is caused by selective v-ATPase inhibition by Tyr^{682} phosphorylated APP βCTF

Eunju Im[1,2], Ying Jiang[1,2], Philip Stavrides[1], Sandipkumar Darji[1], Hediye Erdjument-Bromage[3,7], Thomas A. Neubert[3,7], Matteo Bordi[1,#], Jun Yong Choi[5,6], Ju-Hyun Lee[1,2], and Ralph A. Nixon[1,2,3,4,*]

[1]Center for Dementia Research, Nathan S. Kline Institute, Orangeburg, NY 10962, USA; Departments of [2]Psychiatry and [3]Cell Biology, NYU Grossman School of Medicine, New York, NY, 10016, USA.; and [4]NYU Neuroscience Institute, New York, NY 10016, USA; [5]Department of Chemistry and Biochemistry, Queens College, Queens, NY 11367, USA; [6]Ph.D. Programs in Chemistry and Biochemistry, The Graduate Center of the City University of New York, New York, NY 10016, USA; [7]Kimmel Center for Biology and Medicine at the Skirball Institute, NYU Grossman School of Medicine, New York, NY, 10016, USA.

[*]Correspondence: Ralph.Nixon@nki.rfmh.org

Current address: University of Rome Tor Vergata, Via Cracovia, 50, 00133 Roma RM, Italy

SUMMARY

Lysosome dysfunction arises early and propels Alzheimer's Disease (AD). Herein, we show that amyloid precursor protein (APP), linked to early-onset AD in Down Syndrome (DS), acts directly via its β-C-terminal fragment (βCTF) to disrupt lysosomal v-ATPase and acidification. In human DS fibroblasts or brains of DS model mice, the phosphorylated ^{682}YENPTY internalization motif of APP-βCTF binds selectively within a pocket of the v-ATPase V0a1 subunit cytoplasmic domain and competitively inhibits its association with the V1 subcomplex of v-ATPase. Inhibiting FYN, a mediator of APP Tyr^{682} phosphorylation which is over-active in AD and DS, restores normal v-ATPase and lysosome function in DS fibroblasts and DS model mice. Notably, lowering APP-βCTF or APP Tyr^{682} phosphorylation below normal baseline levels boosts v-ATPase assembly and acidification, suggesting that v-ATPase may also be modulated tonically by phospho-APP-βCTF. These findings offer insight into pathogenic mechanisms also relevant to late onset AD.

Keywords: APP-βCTF, v-ATPase, Down Syndrome, Fyn kinase, Lysosome, Acidification, Phosphorylation, Autophagy, Alzheimer's disease

INTRODUCTION

The ultrastructural neuropathology of Alzheimer's disease (AD) is dominated by robust and selective buildup of autophagic vacuoles within neurons, reflecting the defective transport and clearance of autophagic waste from neurons (Knopman et al., 2021; Nixon, 2013). Abnormalities at all levels of the endosomal-lysosomal-autophagy network are an invariant early and progressive feature of AD neuropathology and pathophysiology (Knopman *et al.*, 2021). Accumulation of APP-βCTF in lysosomes is also believed to corrupt their functioning in AD and Down Syndrome (DS) mouse models and promote AD-related pathology (Jiang et al., 2019; Lauritzen et al., 2016; Tamayev et al., 2012).

The close association between lysosomal dysfunction and neurodegeneration is underscored by mutations of at least 30 genes operating within the endosomal-lysosomal system that cause inheritable neurodegenerative diseases across the aging spectrum (Nixon, 2013; Nixon et al., 2008). In AD, disrupted lysosome function contributes to neuritic dystrophy, reduced clearance of β-amyloid and tau, synaptic plasticity deficits, and neurodegeneration (Cataldo et al.,

2004; Checler et al., 2021; Nixon, 2007; Wang et al., 2009). These deficits in mouse models are substantially remediated by restoring lysosomal functionality (Boland et al., 2018; Hwang et al., 2019; Lee et al., 2019). Despite the growing evidence implicating lysosomes in pathogenesis in neurodegenerative diseases, the mechanisms underlying lysosomal system dysregulation remain unclarified.

Lumenal acidification to a pH of 4.5-5.0 is essential for lysosomal function (Mindell, 2012), including optimal activation of varied hydrolytic enzymes and regulation of ion channels involved in lysosomal trafficking and cell signaling (Ballabio and Bonifacino, 2020; Luzio et al., 2007). Lysosomal acidification is maintained primarily by a vacuolar (H^+)-ATPase (v-ATPase), a multimeric enzyme complex that pumps protons from the cytosol into the lysosomal lumen (Luzio *et al.*, 2007; Mindell, 2012). Fourteen protein subunits form the complete v-ATPase complex comprised of two sectors: an integral membrane-associated V0 sector and a cytosolic V1 sector capable of regulated dissociation from the V0 sector. The V1 sector, comprising subunits A-H, is responsible for ATP hydrolysis. The V0 sector, composed of subunits a, d, e, c, and c'', forms the channel that conducts proton transport (Cotter et al., 2015; Forgac, 2007).

v-ATPase activity is subject to various forms of regulation that modulate subunit expression, assembly, trafficking, and signaling (Cotter *et al.*, 2015). Among the most important is regulation of the V1 sector association with the membrane-bound V0 sector (Liberman et al., 2014; Nakamura, 2004; Stransky and Forgac, 2015). Physiological changes in v-ATPase activity modulate nutrient sensing that controls mTOR activity, autophagy induction, and lysosomal biogenesis (Ballabio and Bonifacino, 2020; Mortimore and Schworer, 1977; Zoncu et al., 2011). Mutations of v-ATPase subunits cause nearly a dozen familial degenerative diseases, most having a significant CNS component (Colacurcio and Nixon, 2016). Notably, this list includes familial early-onset AD due to *PSEN1* mutation, which disrupts maturation and lysosomal delivery of v-ATPase V0a1 subunit, thus impairing v-ATPase assembly and proton pumping, leading to diverse features of AD pathophysiology (Lee et al., 2010).

In this study, we show that *APP*, like *PSEN1* in AD, disrupts v-ATPase complex assembly and lysosomal acidification by a distinctive mechanism that also involves the V0a1 subunit directly. We demonstrate that the Tyr^{682} phosphorylation of APP-βCTF selectively and directly interacts with the cytoplasmic domain of the V0a1 subunit, thereby impeding association

of V1 subunits and inhibiting v-ATPase activity. We further identify a pathogenic role of over-active Fyn kinase in boosting Tyr^{682} phosphorylation of APP in DS as well as AD mouse models and show that lowering APP Tyr^{682} phosphorylation by inhibiting Fyn prevents the disruptive effects of APP-βCTF on lysosome function *in vivo*. Our results and growing evidence on AD pathobiology support our view that v-ATPase disruption is a critical triggering mechanism arising early in AD and that v-ATPase dysregulation is a new therapeutic target. Finally, our initial evidence that lowering APP levels or APP-βCTF itself below baseline endogenous levels accentuates v-ATPase assembly and activity, raises the possibility of tonic modulation of lysosomal function by APP in physiological states as well as in disease. Our findings reported here and other emerging data (Checler *et al.*, 2021) (Lee *et al.*, 2022, in press) point toward a unifying pathogenic mechanism underlying the origin of lysosomal dysfunction in AD.

RESULTS

Lysosomal v-ATPase dysfunction is caused by impaired complex assembly in DS fibroblasts

We confirmed that lysosomal acidification is impaired in Down Syndrome (DS) fibroblasts (Jiang *et al.*, 2019) by measuring lysosomal pH using LysoSensor™ Yellow/Blue dextran, a ratiometric dye targeted to lysosomes (Diwu et al., 1999). Lysosomal pH was significantly increased in DS fibroblasts compared to control (2N) (Figure 1A). Since lysosome acidity is generated mainly by v-ATPase (Mindell, 2012), we measured lysosomal v-ATPase activity by using a superparamagnetic chromatography isolation procedure (Walker and Lloyd-Evans, 2015) to isolate highly enriched lysosomal preparations from DS and 2N cells, the purity of which is reflected by the high level of LAMP1 enrichment (Figure S1A). We then measured the rate of ATP hydrolysis in purified lysosomes monitored by release of inorganic phosphate, which revealed ~40% lower rates in lysosomes isolated from DS fibroblasts relative to 2N (Figure 1B). To confirm the predicted impact of this lowered ATP hydrolysis, we measured the rates of proton translocation into the lysosomal lumen using the quenching of 9-amino-6-chloro-2-methoxyacridine (ACMA), which uncovered a ~80% lower rate in purified lysosomes from DS fibroblasts than from 2N lysosomes (Figures 1C and 1D).

The v-ATPase complex is only active when the membrane-bound V0 sector and the cytosolic V1 sector are assembled on the lysosomal membrane (Stransky and Forgac, 2015). We examined the assembly of the v-ATPase complex using native polyacrylamide gel electrophoresis (PAGE) followed by mass spectrometric (MS) analysis. On native PAGE gels, the fully assembled v-ATPase was present at significantly reduced in DS fibroblasts as compared to 2N cells (Figures 1E and 1F; "Full") and instead, DS cells contained an increased proportion of subcomplexes (Figures 1E, 1F; "Sub"). The bands of v-ATPase were detected with a V1B2 subunit antibody and shown by MS analysis to contain all V1 subunits (Figures S1B and S1C). To investigate a possible disruption of v-ATPase assembly in DS cells, we used an additional approach. We examined the v-ATPase complex assembly on cell membranes separated from the cytosol, each subjected to immunoblot analysis. Importantly, the membrane (Memb):cytosol (Cyto) ratios for all of the V1 subunits were significantly lowered in DS fibroblasts (Figures 1G and 1H).

We next investigated v-ATPase assembly and function using lysosome enriched (Lyso) fractions, which indeed demonstrated a disproportionate v-ATPase deficit relative to the total cellular v-ATPase pool. All V1 subunits in purified lysosomes from DS fibroblasts were present at markedly decreased levels compared to those in the Lyso fraction from 2N cells (Figures 1I and 1J). Importantly, these findings on isolated lysosomes were confirmed by further results from double-immunofluorescence labeling analyses that revealed strong colocalization of V1D subunit with cathepsin B (CTSB)-positive compartments in 2N cells (Figure 1K). Quantitative analyses of colocalization with lysosomes showed a significantly decreased V1D level in DS fibroblasts (Figure 1L). We confirmed lysosomal pH, v-ATPase activity and assembly, and localization of V1 subunits in another aged group (5 month) of DS fibroblasts compared to age matched control (2N) fibroblasts (Figure S2).

Taken together, the foregoing data indicated that dysfunction of v-ATPase activity is caused by a markedly lowered association of the V1 sector with the V0 sector on lysosomal membranes in DS fibroblasts.

APP-βCTF modulates v-ATPase activity and is inhibitory at elevated levels in DS

In light of previous studies linking βCTF to lysosomal dysfunction in AD, DS, and AD models (Bordi et al., 2016; Jiang *et al.*, 2019), we investigated whether the mechanism of the

underlying lysosomal v-ATPase deficits in DS fibroblasts was due to elevated generation of APP-βCTF from the extra APP gene copy (3N). We knocked down APP expression to levels below those in 2N control cells using small interference RNA constructs specifically against human *APP* (siAPP) and compared these cells to those exposed to scrambled RNA sequences (siNC). Knock-down (KD) of APP, confirmed by western blot (WB) 72 hr after siRNA transfection, significantly rescued lysosomal pH (Figure 2A) and v-ATPase activity (Figure 2B) in DS fibroblasts. Moreover, the same treatment restored assembly of the v-ATPase complex (Figures 2C and 2D) with a full complement of V1 subunits (Figures 2E and 2F) in DS fibroblasts. These data therefore indicate that, even in the presence of the entire extra copy of Chr.21 in DS cells, v-ATPase dysfunction is dependent mainly on the extra copy of APP. Unexpectedly, KD of APP in 2N fibroblasts further lowered lysosomal pH by 0.11 pH units which was associated with significantly higher v-ATPase activity (16%). Moreover, levels of V1 subunits associated with lysosomes were significantly higher while corresponding levels in the cytosol were lowered, consistent with an increased assembly of v-ATPase complex on lysosomes. These findings in 2N fibroblasts and additional data discussed later suggest that v-ATPase may be tonically modulated by APP.

APP-βCTF levels are elevated in AD and DS brain (Kim et al., 2016; Pera et al., 2013) and accumulate selectively in lysosomes (Jiang *et al.*, 2019; Lauritzen *et al.*, 2016). We observed that such increases in DS fibroblasts (Jiang *et al.*, 2019) are accompanied by lysosomal pH elevation (Figure 3A). Here we addressed the specificity of APP-βCTF as a mediator of this effect by first measuring v-ATPase activity in lysosomes from cells treated with vehicle or γ-secretase inhibitor L685,458 (γ-Sec INH), which elevates APP-βCTF levels (Figure S3A) by inhibiting its γ–cleavage to form Aβ peptide (Jiang et al., 2010). In 2N cells, γ-Sec INH elevated APP-βCTF levels and strongly inhibited v-ATPase activity (Figure 3B). In DS fibroblasts where APP-βCTF is already elevated and v-ATPase activity is disrupted, an additional impact of γ-Sec INH was not detected (Figure 3B). We observed the same pattern after γ-Sec INH (i.e., DS phenotype induced in 2N cells but minimal effect on DS cells), when assembly of lysosomal v-ATPase was assessed by native gel analysis (Figures 3C and 3D) or CTSB and V1D colocalization was assayed by double-label IFC (Figures 3E and 3F).

In contrast to effects of γ-Sec INH, lowering APP-βCTF generation from APP by using BACE1 inhibitor IV (BACE INH) (Figure S3B) almost fully recovered lysosomal pH (Figure 3A) and function of v-ATPase in DS fibroblasts (Figures 3B-3F). Further supporting the concept that APP may tonically modulate v-ATPase activity, v-ATPase function was enhanced by BACE INH, similar to observations in the siAPP studies (Figure 2B), ATPase activity rose significantly (50%) above baseline activity in BACE INH-treated 2N cells (Figure 3B) and significantly enhanced v-ATPase complex assembly (Figures 3C and 3D) and V1D colocalization with CTSB-positive lysosomes (Figures 3E and 3F). Furthermore, lysosomal pH trended non-significantly toward a lower than baseline acidity (Figure 3A). Finally, to rule out an effect of APP-βCTF on v-ATPase function, we blocked its generation in cells using the selective β-secretase inhibitor TAPI-1 (Hoey et al., 2009), which reduced βCTF levels by 30-50% (Figure S3C). No discernible changes of lysosomal pH (Figure S3D), ATPase activity or v-ATPase assembly (Figures S3E-S3G) were seen in 2N and DS fibroblasts after exposure to TAPI-1.

Taken together, the foregoing data indicated that v-ATPase is specifically regulated by APP-βCTF and suggested that the baseline level of v-ATPase function in 2N fibroblasts reflects a tonic balance that can be potentially modulated by APP-βCTF levels.

APP-βCTF binds selectively to v-ATPase subunits via its YENPTY domain and is dependent on Tyr^{682} APP phosphorylation

A previous synaptic interactome analysis of the APP intracellular domain (AICD) revealed APP-interacting proteins including several v-ATPase subunits, such as V0a1, V0d1, V1A, V1B2, V1C, V1D, and V1E (Del Prete et al., 2014). Based on this clue, we investigated whether APP interacts with v-ATPase subunits by performing co-immunoprecipitation (IP) analyses in 2N and DS fibroblasts. In 2N cell lysates, V0a1, V0d1, V1A, V1B2, V1D, and V1E1 were pulled down in IP using C1/6.1 antibody against the extreme C-terminal sequence of APP (amino-acid residues 676-695 of human APP 695 isoform) (Figures 4A and 4B). The binding affinity of APP with V1 subunits (V1A, V1B2, V1D, and V1E1) decreased in DS fibroblasts (Figure 4B), while APP strongly interacted with V0 subunits (V0a1 and V0d1) (Figure 4A). To establish a lysosomal localization of the interaction between APP and v-ATPase subunits, we performed IP assays using a Lyso fraction. APP showed elevated interaction with V0a1/V0d1 in the Lyso fraction of DS fibroblasts (Figure 4C). By contrast, APP does not interact with V1

subunits (V1A, V1B2, V1D, and V1E1) in the Lyso fraction (Figure 4C). Next, to test whether V0 subunit interacts with flAPP or βCTF, we performed IP assays using V0a1 antibody. V0a1 pulled down APP-βCTF, but not flAPP (Figure 4D). In addition, we confirmed the increased interaction between APP-βCTF and V0a1 in DS fibroblasts compared with 2N cells using proximity ligation assay (PLA; Duolink) (Figures 4E and 4F).

The C-terminal region of APP contains the ^{682}YENPTY internalization motif with an NPXpY element, a typical internalization signal for membrane proteins (Ando et al., 2001). The conserved motif is important for interactions with specific cytosolic proteins, including Fe65-PTB2 and Grb2-SH2 that regulate APP metabolism and signaling (Das et al., 2011; Radzimanowski et al., 2008). Among three Tyr residues present in the AICD, only Tyr^{682} is phosphorylated *in vivo* (Das *et al.*, 2011) and, notably, this phosphorylation is significantly increased in AD brain (Iannuzzi et al., 2020; Russo et al., 2001). To predict the interaction between V0a1 and ^{682}YENPTY motif, we synthesized an unphosphorylated peptide (QNGYENPTY, Pep-1), a phosphorylated peptide (QNG^{P}YENPTY, Pep-2), and a control peptide (QNG^{P}YENVTY, Pep-3) expecting to lose binding affinity to partner proteins due to a conformation change caused by the loss of β-turn conformation at pY+3 (Das *et al.*, 2011). Cell lysates from 2N and DS fibroblasts were incubated with each peptide, and then IP with C1/6.1 antibody. The increased APP binding with V0a1 in DS fibroblasts was decreased by only Pep-2 and occurred in a dose dependent manner (Figure 4G). In addition, treatment of 2N fibroblasts with Pep-2, but not Pep-1, mimicked the effect of βCTF elevation in raising the pH of lysosomes to the abnormally high pH in DS fibroblasts (Figure 4H). Investigation of Aβ_{1-42} peptide under the same conditions revealed no effect on binding of APP with V0 subunits or lysosomal pH (Figures S4A and S4B). To confirm specific interaction between phosphorylated APP and v-ATPase subunits, we carried out a series of co-IP analyses using anti-APP (phospho-Tyr^{682}; pY682) antibody. The binding affinity of pY^{682}CTF with V0a1 subunit was increased in DS fibroblasts (Figure 4I).

Based on the results, we analyzed a known AICD structure complexed with Grb2-SH2 (PDB ID: 3MXC) (Das *et al.*, 2011) to find the binding region in the V0a1 subunit. The phosphate unit of Tyr^{682} is projected toward a pocket composed of R67, R86, S88, S90, S96, and K109 (Figure S4C). The phosphate group forms a hydrogen bonding with S88, S90, and S96 and

salt bridge with R67 and R86. Three methylene units of K109 show π - hydrophobic contact with the phenyl ring of Y682 (Figure S4C). Thus, the structural features of the phospho-Y (pY) binding pocket provide for electrophilic and hydrophobic interactions and stabilize the pY in the pocket. The V0a1 subunit of v-ATPase (PDB ID: 6VQ7), defined from a cryo-electron microscopy (cryo-EM) structure, was analyzed to locate the potential binding site of the pYENPTY motif (Abbas et al., 2020). The cryo-EM structure includes an unsolved region from residue 667 to 712 in the V0a1 subunit, and it possesses three consecutive serine residues (S151, S152, and S153) which are highly conserved among species (Figure S4E). In addition, a basic residue, R198, is located in the middle of the N- and C-terminals of the unsolved region (Figure S4D). Thus, we speculated that this region could form a potential binding pocket for the pYENPTY motif. Moreover, two of three serine residues of the loop could be a part of the binding pocket and provide hydrogen bonding to the phosphate group of the tyrosine residue. Molecular modeling, molecular dynamics (MD) simulation, and docking studies were iteratively conducted to build the pocket and estimate the binding pose of the pYENPTY motif (Case et al., 2005; Halgren et al., 2004). The model structure shows that the phosphate group of pY possesses hydrogen bonding with S151, S153, and T250 and has a salt bridge interaction with R198 (Figures 4J and 4K). The phenyl ring of pY forms hydrophobic contacts with the methylene units of R167 and F170 in a way similar to that shown for the Grb2-SH2 and AICD complex (Figure S4C). Furthermore, MD simulation followed by MM-GBSA calculation (Tsui and Case, 2000) shows the estimated binding affinity of the phosphorylated peptide to the pocket is more stable than its unphosphorylated counterpart ($\Delta\Delta G_{bind}$ = -85.6 kcal/mol versus -67.8 kcal/mol).

Taken together, these analyses strongly suggest that APP-βCTF interacting specifically with V0a1 modulates docking of the V1 sector to V0 and that Tyr^{682} phosphorylation on the ^{682}YENPTY motif of APP plays a crucial role in this interaction.

Inhibition of Fyn kinase mediating APP Tyr^{682} phosphorylation rescues v-ATPase dysfunction in DS

Several tyrosine kinases in brain are known to phosphorylate Tyr^{682} of APP, including ABL1 (Zambrano et al., 2001), TrkA (Tarr et al., 2002), and Fyn kinase (Hoe et al., 2008). To identify candidate kinases possibly involved in v-ATPase dysfunction via Tyr^{682} phosphorylation in DS fibroblasts, we measured mRNA levels of these three kinases. Among these kinases, only

Fyn kinase was increased in DS fibroblasts (Figure 5A). Of greatest relevance to our study, Fyn binds the ^{682}YENPTY motif of APP and alters the trafficking of APP via increased APP Tyr phosphorylation in AD neurons (Poulsen et al., 2017). As expected, elevated levels of Fyn protein were found in DS fibroblasts (Figure 5B). Furthermore, intermolecular auto-phosphorylation of Tyr^{420} that stabilizes the active state of the catalytic site (Kramer-Albers and White, 2011), was increased in DS fibroblasts (Figure 5B), with resultant elevated level of Tyr^{682} phosphorylation of APP-βCTF in DS cells (Figure 5B).

Next, we investigated a possible role of Fyn in mediating v-ATPase dysfunction in DS fibroblasts by testing whether Saracatinib (AZD0530; Fyn INH), a Src family of nonreceptor tyrosine kinases inhibitor with high potency for Fyn, could rescue v-ATPase deficits. Testing with various concentrations of AZD0530 revealed a reduction of phospho-Y^{420}-Fyn (pFyn) at 2 μM AZD0530 (Figure S5A). Next, measurements of lysosomal pH and v-ATPase activity in 2N and DS fibroblasts after treating with or without Fyn INH demonstrated rescue of elevated lysosomal pH, v-ATPase activity deficits, and reduced lysosomal targeting of V1D (Figures 5C-5F) in AZD0530 treated DS fibroblasts showing lowered pFyn (Figure 5C). In addition, decreased interaction between V0a1 and APP-βCTF was also demonstrated in DS fibroblasts treated with AZD0530 (Figure 5G).

To further probe the specific effect of Fyn kinase on the assembly of v-ATPase, small interference RNA constructs specifically against human Fyn (siFyn) were used to KD the expression of Fyn (Figure S5B). As expected, siFyn, but not siNC, restored the lysosomal acidification (Figure 5H), v-ATPase activity (Figure 5I), and lysosomal targeting of V1D (Figures 5L and 5M) in DS fibroblasts. Fyn knockdown also induced reassembly of disrupted V0/V1 complexes in DS fibroblasts (Figures 5J and 5K).

Collectively, these data indicated that the dysfunction of v-ATPase in DS fibroblasts is likely mediated by over-activation of Fyn kinase and its function can be restored by inhibiting Fyn kinase activity with AZD0530.

DS model mice exhibit v-ATPase dysfunction reflecting impaired V0-V1 sector association

We next extended our observations *in vivo* by investigating the possibility of similar lysosomal v-ATPase dysfunction and defective acidification in the Ts2 mouse model of DS

(Jiang *et al.*, 2019). To monitor lysosomal acidification *in vivo*, we crossed Ts2 mice with Thy1 mRFP eGFP LC3 (TRGL6) mice to yield (Ts2*TRGL) mice as described previously (Lee *et al.*, 2019). Introduction of a third fluorescence probe by immunocytochemical labeling with cathepsin D (CTSD) antibody enabled us to detect lysosomes and autolysosomes (AL), and based on their acidification state to discriminate LC3-positive AL that had fused with lysosomes but not acidified from LC3-positive autophagosomes. A computer assisted unbiased measurement of hue angle (an index of wavelength) of individual vesicles that could be triple fluorescent to assign the color of vesicles enabled a relative vesicle pH and objective assignment of vesicle identity (Lee *et al.*, 2019). The confocal images were collected from neocortex sections of 6-9 months old Ts2*TRGL and age-matched TRGL mice (Figure 6A). In Ts2*TRGL mice, numbers of fully acidified AL (purple puncta) were decreased compared to that in control TRGL mice, whereas poorly acidified AL (white puncta) increased in number (Figure 6B). Next, to assess lysosomal v-ATPase activity in these mice, we performed biochemical fractionations to obtain Lyso fractions using an iodixanol step gradient (Figure S6). WB analysis using various organelle markers identified Lyso within fractions 15-18 (Figure S6; Lyso), while measurements of the ATP-hydrolytic activity in this enriched lysosome fraction revealed a ~50% lowered ATP hydrolysis rate in the lysosomes from Ts2 mice relative to those in 2N control mice (Figure 6C).

To confirm disrupting of v-ATPase assembly in Ts2 mouse, we performed native PAGE analysis using membrane fraction. Native PAGE analysis showed that the fully assembled v-ATPase was significantly reduced in the Ts2 mouse, compared with 2N (Figures 6D and 6E). We also performed Western blot analysis using iodixanol step gradient samples, to investigate whether lysosomal targeting of v-ATPase subunits to lysosomes was also disrupted in Ts2 mice. V1 subunits in Lyso (L+) from Ts2 mouse brain were present at markedly decreased levels compared to those in 2N and were increased in other fractions (Lyso-; L-) (Figures 6F and 6G). Consistent with our foregoing results, V0 subunit levels in the Lyso fraction were not changed, as expected (Figures 6F and 6G).

Lysosomal dysfunction in DS model mice is mediated by over-active Fyn and reversed upon Fyn inhibition

We next investigated the phosphorylation of APP-βCTF at Tyr^{682} by Fyn kinase using WB analysis with Tyr phosphorylation specific antibodies in DS model mice. We showed levels

of APP-βCTF (pY^{682}CTF) to be nearly 2-fold higher in Ts2 mouse brain and full-length APP (pY^{682}flAPP), and Fyn (pY^{420}Fyn) to be modestly though significantly increased (Figures 7A and 7B). To further investigate effects of Fyn kinase inhibition *in vivo,* we then treated Ts2 mice with vehicle or 5 mg/kg/day AZD0530 (Fyn INH) by oral gavage for 4 weeks (Kaufman et al., 2015). We confirmed by WB analysis that AZD0530 decreased pFyn levels in Ts2 mice (Figures 7C and 7D) and observed that Fyn kinase inhibition by AZD0530 in Ts2 mice *in vivo* significantly rescued abnormal lysosomal acidification (Figures 7E and 7F) compared to the vehicle treated (Veh) condition and abnormal v-ATPase activity was restored (Figure 7G). In addition, inhibition of Fyn kinase activity in Ts2 mice restored normal levels of the full v-ATPase complex in Ts2 mouse brain (Figures 7H and 7I) and increased association of V1 subunits in Lyso fractions (Figures 7J and 7K). Notably, supporting our foregoing findings on the modulation of v-ATPase at endogenous APP levels, Fyn inhibition in wild-type mice induced supra-normal levels of v-ATPase activity and proportions of full v-ATPase complex in enriched lysosome fractions and an increased proportion of V1 subunits associated with the V0 sector on lysosomes.

The foregoing results establish lysosomal v-ATPase dysfunction in DS model brain *in vivo* as well as in authentic DS in fibroblasts from individuals with DS. We further demonstrate its dependence on Tyr^{682} phosphorylation of APP, which is mediated at least in part by the AD/DS-related elevation of FYN kinase.

v-ATPase deficits are associated with Tyr^{682} APP phosphorylation in APP-based mouse models of AD

As an initial extension of our findings in DS to early onset AD models induced by *APP* or *APP/PSEN1* mutations, we investigated the relevance of Tyr^{682}APP phosphorylation to defective lysosomal acidification and function in two AD mouse models: 6-month-old 5xFAD mice exhibiting early-onset amyloidosis (at 2 months) and 6-month-old Tg2576 mice with a later age of onset (at 10-12 months). v-ATPase activity measured in Lyso fractions was reduced by ~45% in each model relative to WT controls (Figures S7A and S7F). Phosphorylation of APP at Tyr^{682} is increased in AD brain (Guenette et al., 2017; Russo *et al.*, 2001) and is also associated with higher Fyn kinase activity (Iannuzzi *et al.*, 2020). Accordingly, we found levels of phosphorylation of APP-βCTF and flAPP at Tyr^{682} to be over 3-fold higher in Tg2576 mouse

brain, and the phospho-Tyr^{420} form of Fyn kinase to be nearly 12-fold increased (Figures S7B and S7C). Levels of pY^{682}CTF (Figure S7D) or pY^{682}flAPP (Figure S7E) showed a high positive correlation with Fyn kinase activity (pY^{420}Fyn) compared with WT (blue) and Tg2576 (red) (Figures S7D and S7E). Similar results were also observed in brains of 5xFAD (Figures S7G-S7J).

DISCUSSION

In all forms of AD, the impaired clearance of autophagic and endocytic substrates by lysosomes causes profuse accumulations of neuronal waste, including the build-up in lysosomes of key APP metabolites (eg. βCTF, Aβ), ultimately leading to lysosomal membrane permeability and neuronal cell death (Almeida et al., 2020; Česen et al., 2012; Nixon and Yang, 2012) (Lee *et al.*, 2022, in press). In this report, we have established an APP-dependent primary mechanism underlying lysosome dysfunction in DS, the genetic congenital disorder leading to the most prevalent form of early onset AD (Colacurcio et al., 2018; Doran et al., 2017; Lott and Head, 2019). Lysosomal v-ATPase function is disrupted by APP-βCTF directly interacting with the critical membrane-anchored V0a1 subunit of v-ATPase thereby impeding assembly of the V1 sector into the V0 sector of v-ATPase. Notably, mutations of *PSEN1*, a major cause of early-onset AD (De Strooper, 2007), also impact V0a1 by impeding the ER chaperone role of presenilin 1 holoprotein required for glycosylation and stability of nascent V0a1 subunits and there adequate delivery to lysosomes (Lee et al., 2015; Lee *et al.*, 2010). These findings and others, therefore, highlight V0a1 as a common disease target in AD.

We further establish here that Tyr^{682} APP phosphorylation is critical for the selective pathogenic interaction of phospho-variant Tyr^{682}APP-βCTF with V0a1. Our molecular modeling studies showed that only the phospho-Tyr^{682} variant of APP-βCTF, through its conserved YENPTY motif, has strong affinity to a structural pocket in the V0a1 cytoplasmic domain and the predicted interaction was confirmed in co-IP studies with peptide analogues. The interaction impedes the V1 subcomplex that mediates ATPase activity from assembling efficiently with the membrane-anchored V0 sector, thereby inhibiting full v-ATPase complex assembly, lysosomal ATPase activity, proton pumping, and lysosomal acidification (Figures 4 and 5). The modestly elevated level of endogenous APP-βCTF in DS (Cataldo et al., 2008) is necessary and *sufficient*

to raise lysosomal pH and partially inactivate lysosomal enzymes, as these pathological consequences are reversed by reducing APP-βCTF levels (Jiang *et al.*, 2019) either directly or via BACE1 inhibition, which also lowers phospho-Tyr^{682} APP-βCTF levels. Alternatively, reversal could also be achieved by inhibiting the activity of Fyn kinase, which targets Tyr^{682} on APP and is over-active in DS (Ho et al., 2005; Nygaard et al., 2014; Shirazi and Wood, 1993). Our key findings on DS are validated both in the authentic human disorder (primary fibroblasts from individuals with DS), and in brains of adult DS model mice *in vivo*.

The pathogenic binding to v-ATPase is an effect of APP-βCTF, but not Aβ or APP-CTF, based on our use of γ- and -secretase inhibitors and peptide competition assays with v-ATPase subunits. Brain levels of APP-βCTF are not only elevated in DS but also in individuals with familial Alzheimer's Disease (FAD) caused by APP or PSEN1 mutations (De Jonghe et al., 2001; Jiang *et al.*, 2019; Kim *et al.*, 2016; Pitsi and Octave, 2004; Salehi et al., 2006) and in IPSCs derived from homozygous APOE4 carriers (Woodruff et al., 2016). In DS, expression of the AD phenotype of endosomal and lysosomal anomalies (Jiang *et al.*, 2019; Kim *et al.*, 2016; Salehi *et al.*, 2006) is dependent on a single extra copy of APP, highlighting the sensitivity of the v-ATPase system response to modest APP-βCTF elevations. Levels of Fyn kinase and Tyr^{682} phosphorylated APP and APP-βCTF in brain are also elevated in individuals with late-onset "sporadic" AD (Holsinger et al., 2002; Iannuzzi *et al.*, 2020; Russo *et al.*, 2001) as well as in two different AD model mice (Tg2576 and 5xFAD), and the levels correlated with Fyn kinase activation (pTyr^{420}Fyn) (Figures S7B-S7E and S7G-S7J).

The foregoing mechanisms are potentially relevant to explaining the similar lysosomal dysfunction in sporadic AD. In late-onset (sporadic) AD, such elevations of APP-βCTF, in the absence of a rise in APP levels, could result from multiple factors and be additive. These include an increased level of BACE1 activity (Li et al., 2004; Yang et al., 2003; Zuliani et al., 2020), Tyr^{682} APP phosphorylation, which notably also promotes β-cleavage of APP over alpha-cleavage (Yáñez et al., 2016), and APP processing regulation by GWAS identified AD risk genes such as BIN1, SORL1, ABCA7, and RIN3 (Shen et al., 2020; Wang et al., 2021). Additionally, as hydrolytic efficiency declines in aging due to rising oxidative stress, lipid accumulations, and other aging factors (Butterfield et al., 2014; Nixon, 2020; Perluigi and

Butterfield, 2012), APP-βCTF may well build-up in lysosomes disproportionately to flAPP levels (Tam et al., 2016; Tian et al., 2014) and inhibit ATPase.

Although not the main focus of our analyses on CTF pathogenicity in AD, we observed consistently that manipulations that lowered Tyr^{682} APP-βCTF below normal baseline, induced supra-normal v-ATPase assembly, lysosomal ATPase activity, and acidification. Such conditions included knockdown of APP (Figure 2), BACE1 inhibitor treatment (Figure 3), and reducing levels of Fyn kinase protein or activity (Figures 5 and 6). Collectively, these findings support the possibility that change in APP-βCTF levels in normal lysosomes under varying physiological levels may tonically modulate v-ATPase activity, although implications of such potential modulation, including therapeutic applications, require future investigation.

In conclusion, *APP* in DS joins *PSEN1* as genes that are both causal for early-onset AD and, through direct actions of the protein they encode, they disrupt lysosomal function and autophagy, as is evident in virtually all forms of AD (Nixon and Yang, 2011). Numerous studies of human sporadic AD and APP-based AD mouse models have revealed lysosome/autophagy dysfunction to be among the earliest appearing anomalies in AD and the catalyst for varied downstream pathophysiology associated with AD development (Cataldo et al., 1996; Nixon, 2017) (Lee et al. 2022). Our results unequivocally establish the importance of APP-βCTF in AD etiology by demonstrating a direct pathogenic action of APP-βCTF in DS, the most prevalent form of early onset AD, and by extending the relevance of the mechanism to AD mouse models. Our findings, together with other emerging data, point toward acidification failure within the lysosomal network as a potential unifying pathogenic mechanism in AD, driven by converging genetic, aging, and environmental factors of varying influence depending on the subtype of AD (Butterfield *et al.*, 2014; Colacurcio and Nixon, 2016; Nixon, 2020). Finally, mounting preclinical evidence establishes the ameliorative impact of lysosome re-acidification not only on lysosomal efficacy but on neuropathological signatures, synaptic plasticity, and cognition. As such, acidification rescue represents a promising innovative target for the remediation of lysosome dysfunction in AD and related disorders (Brouillard et al., 2021; Lee et al., 2020; Lie and Nixon, 2019).

ACKNOWLEDGMENTS

This work was supported by NIA P01AG017617 to R.A.N. We thank Dr. Kuglae Kim (Yonsei University, Republic of Korea) for advising from structural analyses. We are very grateful to Dr. Efrat Levy (Nathan S. Kline Institute; NYU Grossman School of Medicine) for supervising animal breeding, and thank Dr. Monica Pawlik, Chunfeng Huo, and Steven DeRosa (Nathan S. Kline Institute) for maintaining animals.

AUTHOR CONTRIBUTIONS

E.I. and R.A.N. were equally responsible for experimental design and data interpretation and mainly contributed to writing and revising the manuscript; E.I. conducted the experiments; P.S. conducted tissue processing and analyzed autolysosome acidity of TRGL mouse; S.D. analyzed RNA-seq data; P.S. and S.D. performed gavage for Saracatinib treatment; H.E.B. and T.A.N. performed mass spectrometry analysis; J.Y.C performed molecular docking and simulation; M.B. and Y.J. provided RNA-seq data from human fibroblasts; E.I., Y.J., J.H.L, P.S., and J.Y.C. contributed to data interpretation and critically read the manuscript.

DECLARATION OF INTERESTS

The authors declare no competing interests.

FIGURE LEGENDS

Figure 1. Assembly of the lysosomal v-ATPase complex is impaired in DS fibroblasts

(A) Lysosomal pH measured ratiometrically using LysoSensor Yellow/Blue (Y/B) dextran. (B-D) Lysosomal v-ATPase activity measured colorimetrically as ATP hydrolysis (*B*) and fluorometrically (ACMA method) as H^+ transport (*C*, *D*) using Lyso fractions. (E) Membrane fractions were resolved using native PAGE. (F) The graph represents ratio of full complex versus total (full plus sub complexes) complexes of v-ATPase. (G) Immunoblots of v-ATPase subunits distribution in cytosol (Cyto.) and membrane (Memb.) fractions. Na, K-ATPase 1 (NKA) served as a Memb. maker, and GAPDH served as a Cyto. marker. (H) The graphs represent ratio of Memb. vs Cyto. band of each v-ATPase subunits. (I) Immunoblot of v-ATPase subunit distributions in total lysates (Total) and lysosome enriched (Lyso.) fractions. LAMP1 served as a marker for lysosomes and Actin served as a loading control for total lysates. (J) The graphs show relative band intensity for each v-ATPase subunit. (K, L) Double-immunofluorescence labeling shows colocalization of v-ATPase (V1D) and cathepsin B (CTSB) (*K*). Scale bar, 10 µm. Quantification analysis of v-ATPase V1D and lysosomal marker, CTSB, shows colocalization in 2N and DS fibroblasts as calculated by Pearson's correlation coefficient ($n \geq 88$ cells) (*L*).

Figure 2. Impairment of lysosomal v-ATPase in DS fibroblasts is dependent on APP expression

(A) Lysosomal pH of 2N and DS fibroblasts transfected with siRNA for either negative control (siNC) or APP (siAPP) for 72 hr determined by LysoSensor Y/B dextran. The immunoblot represents APP levels in 2N and DS fibroblasts after transfection with 40 nM siNC or siAPP. (B) ATP hydrolysis activity of v-ATPase measured using lysosomal fractions from siRNA transfected 2N and DS fibroblasts. (C) Immunoblots of v-ATPase subunit distributions in cytosol (Cyto.) and membrane (Memb.) fractions of siRNA transfected 2N and DS fibroblasts. NKA served as a Memb. marker, and Actin served as a Cytol marker. (D) The graphs represent ratio of Memb. vs Cyto. band of each v-ATPase subunits. (E) Immunoblots of v-ATPase subunit distributions in total and Lyso. fractions of siRNA transfected 2N and DS fibroblasts. LAMP1 served as a Lyso marker and GAPDH served as a loading control for total lysates. (F) The graphs show band intensity of each v-ATPase subunit from Lyso fraction. Statistical significance between groups is shown by symbols: *2N+siNC vs others, #DS+siNC vs DS+siAPP.

Figure 3. Lysosomal v-ATPase activity is specifically affected by APP-βCTF among metabolites of APP

(A) Lysosomal pH of 2N and DS fibroblasts treated with either DMSO (No Tx), γ-secretase inhibitor, L685,458 (γ-Sec INH; 10 μM), or BACE1 inhibitor (BACE INH; 10 μM) for 24 hr determined by LysoSensor Y/B dextran. (B) ATP hydrolysis activity of v-ATPase measured using lysosome fractions from 2N and DS fibroblasts after treatment indicated inhibitors. (C) Membrane fractions from 2N and DS fibroblasts treated with indicated inhibitors were resolved using the native PAGE. (D) The graph represents the ratio of full complex vs total complexes of v-ATPase. (E, F) Double-immunofluorescence labeling shows colocalization of V1D and CTSB in 2N and DS fibroblasts treated with indicated inhibitors (*E*). Scale bar, 10 μm. Quantification analysis of v-ATPase V1D and lysosomal marker, CTSB, shows colocalization in 2N and DS fibroblasts treated with indicated inhibitors as calculated by Pearson's correlation coefficient ($n \geq 85$ cells) (*F*). Statistically significance between groups is shown by symbols: *2N No Tx vs others, #DS No Tx vs DS+inhibitor.

Figure 4. pYENPTY motif of APP-βCTF interrupt the lysosomal pH via interaction with v-ATPase subunits that form a structural pocket within the complex

(A-C) Cell lysates (*A, B*) or Lyso fraction (*C*) were immunoprecipitated (IP) with anti-APP (C1/6.1) antibody, followed by immunoblotting (IB) with antibodies of v-ATPase V0 subunits (*A, C*) and V1 subunits (*B, C*). The values at the bottom of the left IP blot indicate the relative intensities of IP-ed V0a1 and V0d1 normalized by IP-ed flAPP. (D) Cell lysates were IP with anti-V0a1 antibody, followed by IB with anti-APP (6E10). The values at the bottom of the left IP blot indicate the relative intensities of IP-ed βCTF normalized against IP-ed V0a1. (E) *Left panel:* Schematic diagram of v-ATPase complex, APP-βCTF, and Proximity Ligation Assay (PLA). PLA performed using V0a1 antibody and C1/6.1 for APP C-terminus. The red box represents signal of PLA (Duolink). *Right panel:* Representative fluorescent microscopy image of PLA signals demonstrating association of APP with the V0a1. Scale bar, 10 μm. (F) The graph show number (#) of dots per cell. (G) Cell lysates were incubated with varying amounts of each peptide (Pep-1, Pep-2, and Pep-3) for 24 hr, then IP with anti-APP (C1/6.1) antibody, followed by IB with anti-V0a1 antibody. The values at the bottom of the left IP blot indicate the relative intensities of IP-ed V0a1normalized against IP-ed CTFs. (H) Lysosomal pH of 2N and DS

fibroblasts treated with either DMSO (-) or 5 μM peptides for 24 hr determined by LysoSensor Y/B dextran. (I) Cell lysates were IP with anti-pY^{682} APP antibody, followed by immunoblotting with antibody of V0a1. Non-specific Immunoglobulin G (IgG) used as a control IP against 2N cells. Actin and GAPDH served as a loading control and LAMP2 served as a lysosomal marker. (J) *Left panel:* Schematic diagram of binding with V0a1 and pY^{682}APP-βCTF. *Right panel:* The surface of the pYENPTY binding pocket of V0a1. The positions of phosphorylated pYENPTY motif (pY^{682}) and F196 and R167 of V0a1 subunits are labelled. (K) The binding poses of the pYENPTY motif in the pocket of V0a1. Hydrogen bond and salt bridge interactions by S151, S153, R198, and T250 are labeled with yellow dash lines. The methylene units of R167 and F170 form π - hydrophobic contacts with the aromatic ring of the phosphorylated tyrosine. Proline at the pY+3 position has π - hydrophobic interaction with F196. The pYENPTY motif is yellow, and the unsolved region is light blue.

Figure 5. Inhibition of Fyn kinase mediating APP Tyr^{682} phosphorylation rescues v-ATPase dysfunction in DS fibroblasts

(A) mRNA levels of tyrosine kinase in 2N and DS fibroblast. (B) Immunoblots of phospho-Y^{420}Fyn kinase, Fyn kinase, phospho-Y^{682}CTF, and CTFs distribution in total lysates of 2N and DS fibroblasts. (C) Lysosomal pH of 2N and DS fibroblasts treated with either DMSO (-) or 2 μM Fyn kinase inhibitor (Fyn INH) for 24 hr determined by LysoSensor Y/B dextran. Immunoblot represents phospho-Y^{420}Fyn (pFyn) and Fyn kinase protein levels in 2N and DS fibroblast. (D) ATP hydrolysis activity of v-ATPase measured using lysosomal fractions from DMSO or Fyn INH treated 2N and DS fibroblast. (E, F) Double-immunofluorescence labeling shows colocalization of V1D and CTSB in 2N and DS fibroblasts treated with DMSO or Fyn INH (*E*). Scale bar, 10 μm. Quantification of v-ATPase V1D and lysosomal marker, CTSB, shows colocalization in 2N and DS fibroblasts treated with DMSO or Fyn INH as calculated by Pearson's correlation coefficient ($n \geq 118$ cells) (*F*). (G) After treated with DMSO (-) or 2 μM Fyn INH (+), cell lysates were IP with anti-APP (6E10) antibody, followed by IB with anti-V0a1 antibody. (H) Lysosomal pH of 2N and DS fibroblasts transfected with siRNA for either negative control (-) or 100 nM Fyn (+) for 48 hr, as determined by LysoSensor Y/B dextran. Immunoblot represents Fyn kinase protein levels in 2N and DS fibroblast. Actin or GAPDH served as a loading control. (I) ATP hydrolysis activity of v-ATPase measured using lysosomal

fractions from siRNA transfected 2N and DS fibroblast. (J) Membrane fractions from siRNA transfected 2N and DS fibroblasts were resolved using the native PAGE. (K) The graph represents ratio of full complex versus total (full plus partial complexes) complexes of v-ATPase. (L, M) Double-immunofluorescence labeling shows colocalization of V1D and CTSB in siRNA transfected 2N and DS fibroblasts (*L*). Scale bar, 10 µm. Quantification of v-ATPase V1D and lysosomal marker, CTSB, shows colocalization in siRNA transfected 2N and DS fibroblasts, as calculated by Pearson's correlation coefficient (n ≥ 139 cells) (*M*). Statistically significance between groups is shown by symbols: *2N vs others, #DS vs DS+Fyn INH/siFyn.

Figure 6. Defective lysosomal v-ATPase function in Ts2 mouse model

(A, B) Representative fluorescence images of tfLC3 color changes of TRGL or Ts2*TRGL adult brain (*A*) and respective quantification of puncta representing autolysosomes (fully or less acidified) (*B*). For data analysis, color change of tfLC3-positive vesicles was calculated with CTSD co-labeling. Bar colors denote the colors of puncta; purple bars indicate tfLC3 with CTSD (fully acidified ALs, quenched eGFP) and white bars indicate tfLC3 with CTSD (less acidified ALs, unquenched eGFP). (C) ATP hydrolysis activity of v-ATPase measured using Lyso fraction (15-18) of iodixanol step gradient from adult mouse. (D) Membrane fractions were resolved using the native. (E) The graph represents ratio of full vs total complexes of v-ATPase. (F) Adult mouse brain from control (2N) and Ts2 homogenates were fractionated through an iodixanol step gradient. Each fraction (lysosomal enriched fraction [Lyso]: 15-18; exclude lysosomal enriched fraction [Lyso-]: 1-14 & 19-22) and post-nuclear supernatant (PNS) were resolved using the SDS-PAGE and immunoblotted with anti-V1A, V1C1, V1D, V0a1, and V0d1 antibodies. (G) The graphs represent levels of v-ATPase subunits from each fraction.

Figure 7. Inhibiting over-active Fyn kinase *in vivo* reverses v-ATPase dysfunction in brains of DS model mice

(A) Immunoblot represents phospho-APP (pY^{682}CTFs and pY^{682}flAPP), APP (CTFs and flAPP), phospho-Y^{420}Fyn and Fyn kinase levels in 2N and Ts2 mouse brain. (B) The graphs show band intensity of pY proteins. (C) The immunoblot represents phospho-Y^{420}Fyn (pFyn) and Fyn kinase levels in 2N and Ts2 after treated with either vehicle (-) or Fyn INH (+) for 4 weeks. GAPDH served as a loading control. (D) The graphs show band intensity of phospho-Fyn proteins. (E, F) Representative fluorescence images of tfLC3 color changes of adult brain after

treatment with vehicle (Veh) or Fyn INH for 3 weeks (*E*) and respective quantification of puncta representing autolysosomes (fully or less acidified) (*F*). (G) ATP hydrolysis activity of v-ATPase measured using Lyso fraction (15-18) of iodixanol step gradient from adult mouse brain after treatment with vehicle (-) or Fyn INH (+) for 4 weeks. (H) Membrane fractions from Fyn INH treated adult mouse brain were resolved using native PAGE. (I) The graphs represent the ratio of full vs total complexes of v-ATPase. (J) Homogenates from Fyn INH treated 2N and Ts2 adult mice brain were fractionated through an iodixanol step gradient. The Lyso fraction and the PNS were resolved using the SDS-PAGE and immunoblotted using indicated antibodies. (K) The graphs represent levels of lysosomal v-ATPase subunits. Statistically significance between groups is shown by symbols: *2N+Veh vs others, #DS+Veh vs DS+Fyn INH.

MATERIALS AND METHODS

KEY RESOURCES TABLE

REAGENT or RESOURCE	SOURCE	IDENTIFIER
Antibodies		
Mouse anti-APP (C1/6.1)	Mathew et al., 2002	
Mouse anti-APP (6E10)	BioLegend	Cat# 803001; RRID: AB_2564653
Rabbit anti-APP (Phospho-Tyr^{757})	GenScript	Cat# A00697-40; RRID: AB_1108125
Rabbit anti-V0a1	Abcam	Cat# ab176858; RRID: AB_2802122
Rabbit anti-V0b	Abcam	Cat# ab107189; RRID: AB_10865216
Rabbit anti-V0c	Abcam	Cat# ab104374; RRID: AB_10712593
Mouse anti-V0d1	Abcam	Cat# ab56441; RRID: AB_940402
Rabbit anti-V0e2	Abcam	Cat# ab178934; RRID: AB_2892774
Rabbit anti-V1A	GeneTex	Cat# GTX110815; RRID: AB_1949704
Rabbit anti-V1B2	Abcam	ab73404; RRID: AB_1924799
Rabbit anti-V1C1	Abcam	Cat# ab87163; RRID: AB_1951504
Rabbit anti-V1D	Abcam	Cat# ab157458; RRID: AB_2732041
Rabbit anti-V1E1	Abcam	Cat# ab111733; RRID: AB_10861729
Rabbit anti-V1F	Abcam	ab190789; RRID: AB_2892713
Rabbit anti-V1G1	Abcam	Cat# ab174243; RRID: AB_2892716
Rabbit anti-V1H	Abcam	Cat# ab96120; RRID: AB_10679342
Rabbit anti-Fyn	Cell Signaling Technology	Cat# 4023; RRID: AB_10698604
Rabbit anti-phospho-Fyn (Tyr530)	Thermo Fisher Scientific	Cat# PA5-36644; RRID: AB_2553632
Rabbit anti-phospho-Fyn (Tyr420)	MyBioSouce	Cat# MBS9128730; RRID: AB_2892719
Mouse anti-LMAP1	Developmental Studies Hybridoma Bank	Cat# H4A3; RRID: AB_2296838
Mouse anti-LMAP2	Developmental Studies Hybridoma Bank	Cat# H4B4; RRID: AB_2134755
Goat anti-cathepsin B	Neuromics	Cat# GT15047; RRID: AB_2737184
Rabbit anti-Rab5	Abcam	Cat# ab218624; RRID: AB_2892717
Mouse anti-Rab7	Abcam	Cat# ab50533; RRID: AB_882241

Mouse anti-PDI	GeneTex	Cat# GTX22792; RRID: AB_384853
Rabbit anti-Syntaxin 6	Cell Signaling Technology	Cat# 2869; RRID: AB_2196500
Mouse anti-Tubulin	Sigma-Aldrich	Cat# T8535; RRID: AB_261795
Mouse anti-Actin	Sigma-Aldrich	Cat# A1978; RRID: AB_476692
Mouse anti-GAPDH	Millipore Sigma	Cat# CB1001; RRID: AB_2107426
Rabbit anti-Na, K-ATPase alpha	Cell Signaling Technology	Cat# 3010; RRID: AB_2060983
Mouse Normal IgG control	Millipore	Cat# 12-371; RRID: AB_145840
Rabbit Normal IgG control	Millipore	Cat# 12-370; RRID: AB_145841
Peroxidase AffiniPure Donkey Anti-Mouse IgG (H+L)	Jackson ImmunoResearch	Cat# 715-035-150; RRID: AB_2340770
Peroxidase AffiniPure Donkey Anti-Rabbit IgG (H+L)	Jackson ImmunoResearch	Cat# 711-035-152; RRID: AB_10015282
Peroxidase AffiniPure Donkey Anti-Goat IgG (H+L)	Jackson ImmunoResearch	Cat# 705-035-147; RRID: AB_2313587
VeriBlot for IP detection Reagent (HRP)	Abcam	Cat# ab131366; RRID: AB_2892718
Donkey anti-Goat Alexa Fluor 488	Molecular Probes	Cat# A-11055; RRID: AB_2534102
Goat anti-Rabbit Alexa Fluor 568	Molecular Probes	Cat# A-11036; RRID: AB_10563566
Chemicals, peptides, and recombinant proteins		
L-685, 459	Tocris Bioscience	Cat# 2627; CAS: 292632-98-5
β-Secretase inhibitor IV	Calbiochem	Cat# 565788; CAS: 797035-11-1
TAPI-1	Calbiochem	Cat# 579051; CAS: 171235-71-5
Saracatinib (AZD0530)	Selleck Chemical LLC	Cat# S1006; CAS: 379231-04-6
Concanamycin A (ConA)	Sigma-Aldrich	Cat# C9795; CAS: 80890-47-7
DNase I	Sigma-Aldrich	Cat# 10104159001
Halt™ Protease and Phosphatase inhibitor Cocktail (100X)	Thermo Fisher Scientific	Cat# 78444
LysoSensor™ Yellow/Blue dextran	Molecular Probes	Cat# L22460
Dextran conjugated magnetite	Liquid Research LLC	Cat# DexoMAG™40
9-amino-6-chloro-2-methoxyacridine (ACMA)	Sigma-Aldrich	Cat# A5806; CAS: 3548-09-2
OptiPrep™ Density Gradient Medium	Sigma-Aldrich	Cat# D1556; CAS: 92339-11-2
ECL Chemiluminescent Substrate Reagent	Invitrogen	Cat# WP20005
Immobilon Western Chemiluminescent HRP Substrate	Millipore	Cat# WBKLS0500
PureProteome™ Protein A/G Mix Magnetic Beads	Millipore	Cat# LSKMAGAG10

Precision Plus Protein Dual Color Standards	BIO-RAD	Cat# 161-0374
NativeMark™ Unstained Protein Standard	Thermo Fisher Scientific	Cat# LC0725
Digitonin	Sigma-Aldrich	Cat# D141; CAS: 11024-24-1
NativePAGE™ sample buffer (4X)	Invitrogen	Cat# BN2003
NativePAGE™ G-250 sample additive	Invitrogen	Cat# BN2004
NativePAGE™ Running Buffer (20X)	Invitrogen	Cat# BN2001
NuPAGE™ Transfer Buffer (20X)	Invitrogen	Cat# NP00061
32% Paraformaldehyde (PFA)	Electron Microscopy Sciences	Cat# 50-980-494; CAS: 30525-89-4
Duolink® In Situ Red Starter Kit Mouse/Rabbit	Sigma-Aldrich	Cat# DUO92101-1KIT
Lipofectamine™ RNAiMAX Transfection	Invitrogen	Cat# 13778150
Poly-D-lysine	Sigma	Cat# P0899
MEM	Gibco	Cat# 10370088
Opti-MEM	Gibco	Cat# 51985034
Fetal Bovine Serum	Gibco	Cat# 16000069
Horse Serum	Gibco	Cat# 16050-122
Penicillin-Streptomycin (10,000 U/ml)	Gibco	Cat# 15140122
Trypsin-EDTA (0.05%), phenol red	Gibco	Cat# 25300120
QNGYENPTY	GenScript	Custom-designed
QNG(p)YENPTY	GenScript	Custom-designed
QNG(p)YENVTY	GenScript	Custom-designed
Amyloid β_{1-42} peptide	GenScript	Cat# RP10034-1
Trypsin gold	Progema	Cat# V5280
SPE Empore C18 Extraction Disks	Aka Stage Tips	Cat# 2215
Self-packed 75µm x 2 cm reverse phase column; Packing: ReproSil-Pur C18-AQ 3µm	Ammerbuch-Entringen	Cat# r13.aq
Empty PicoTip Emitter	Now Objective Inc	Cat# PF360-75-10-N5
QExactive HF Orbitrap mass spectrometer	Thermo Fisher Scientific	Cat# 05000L-05999L
Nonospray Flex Source	Thermo Fisher Scientific	Cat# ES071
Easy-nLC 1000 nanoflow liquid chromatography (LC) system	Thermo Fisher Scientific	Cat# LC120
Critical commercial assays		
ATPase activity Kit (Colorimetric)	Innova Biosciences (Current: Abcam)	Cat# 601-0120 (Cat# ab270551)
ULTRARIPA® kit for Lipid Raft	Biodynamics Laboratory Inc	Cat# F015
Deposited data		
Mammalian v-ATPase structure from rat brain		PDB: 6VQ7
Structure of Grb2-SH2 domain and AICD peptide complexes		PDB: 3MXC
Experimental models: Cell lines		
Fibroblast from skin, Thorax/abdomen, Trisomy21, 2 YR	Coriell Cell Repositories	AG06922
Fibroblast from skin, Foreskin, apparently healthy individual, 2 YR		AG07095

Fibroblast from skin, Thorax, Trisomy21, 5 MO	Coriell Cell Repositories	AG07096
Fibroblast from skin, Foreskin, apparently healthy individual, 5 MO	Coriell Cell Repositories	GM08680
Experimental models: Organisms/strains		
Mouse: Ts2	Jiang et al., 2019	
Mouse: TRGL6	Lee et al., 2019	
Mouse: TRGL6 x Ts2	This study	
Oligonucleotides		
siRNA against human APP: ACUAGUGCAUGAAUAGAUUCUCUCC UUUGAUCACGUACUUAUCUAAGAGAGG	Integrated DNA Technologies	
siRNA against human Fyn: GGACUCACCGUCUUUGGAGtt ttCCUGAGUGGCAGAAACCUC	Life Technologies Corp.	Silencer Pre-Designed siRNA ID 1442, Cat# AM51331
Negative control DsiRNA: CGUUAAUCGCGUAUAAUACGCGUAT AUACGCGUAUUAUACGCGAUUAACGAC	Integrated DNA Technologies	Cat# 51-01-14-03
Software and algorithms		
FIJI	NIH	https://hpc.nih.gov/apps/Fiji.html
Photoshop 2021	Adobe	
GraphPad Prism 8	GraphPad	https://www.graphpad.com/scientific-software/prism/
Maestro 12	Schrödinger	https://www.schrodinger.com/products/maestro
The PyMOL Molecular Graphics System v2.0	Schrödinger	https://www.schrodinger.com/products/pymol

RESOURCE AVAILABILITY

Lead contact

Further information and requests for resources and reagents should be directed to and will be fulfilled by the lead contact, Dr. Ralph Nixon (Ralph.Nixon@nki.rfmh.org)

Materials availability

Unique reagents and mouse lines generated in this study are available from the lead contact and may require completion of a materials transfer agreement.

Data and code availability

No large datasets or custom code were generated in this study.

EXPERIMENTAL MODEL AND SUBJECT DETAILS

Animals

All animal procedures were performed following the National Institutes of Health Guidelines for the Humane Treatment of Animals, with approval from the Institutional Animal Care and Use Committee at

the Nathan Kline Institute for Psychiatric Research. Four mouse models were used: (1) Control mice (2N), C57BL/6JEi x C3H/HeSnJ; (2) Ts[Rb(12.17^{16})]2Cje (Ts2), carrying a chromosomal rearrangement of the Ts65Dn genome whereby the marker chromosome has been translocated to Chromosome 12 (MMU12) forming a Robertsonian chromosome (Villar et al., 2005), were studied at 6-9 months; (3) TRGL6 (Thy1 mRFP-eGFP-LC3, Line 6), expressing tandem fluorescent mRFP-eGFP-LC3 under individual Thy 1 promoters (Lee *et al.*, 2019); (4) Ts2 x TRGL6, a transgenic Ts2 mouse model expressing tandem-fluorescent mRFP-eGFP-LC3 under individual Thy1 promoters, were studied at 6-9 months; (5) 5xFAD x TRGL6, 5xFAD (Tg6799, C57BL/6NTAC), which express mutant human APP and PSEN1 (APP KM670/671NL: Swedish, I716V: Florida, V717I: London, PSEN1 M146L, L286V) (Oakley et al., 2006), were crossed with TRGL6 and were studied at 6 months together with age-matched controls; (6) Tg2576 (B6;SJF, Tg(APPSWE)2576Kha), expressing mutant human APP (Swedish K670N/M671L) (Hsiao et al., 1996), were studied at 6 months together with age-matched controls. All mice were genotyped by PCR. Mice were group-housed under 12 h light/dark cycle at constant room temperature and provided with food and water ad libitum. Age-matched WT mice of comparable background were used as controls.

METHOD DETAILS

Cell lines and transfection

Human foreskin fibroblasts from Down syndrome patient (DS) and diploid age-matched controls (2N) were purchased from the Coriell Cell Repositories (AG06922, AG07095, AG07096, GM08680) and maintained according to the distributor's protocols (http://ccr.coriell.org/). Throughout this study, fibroblasts were used below passage number 15 to keep the original character and morphology.

siRNA against human APP and negative control DsiRNA were purchased from Integrated DNA Technologies (IDT) and used as previously described (Jiang *et al.*, 2010). siRNA against human Fyn was purchased from Life Technologies Corp. Cells were transfected using Lipofectamine RNAiMAX according to the manufacturer's protocol.

Ts2 x TRGL mouse generation

For the generation Ts2 x TRGL6 mice, Ts2 mice were bred with our previously described TRGL6 (***T****hy1* m**R**FP-e**G**FP-**L**C3, Line **6**) transgenic mice expressing tandem fluorescent mRFP-eGFP-LC3 (Lee *et al.*, 2019). Ts2*TRGL mice were studied at 6-9 month together with age-matched controls. Mice used in this study were maintained according to Institutional Animal Care and Use Committee guidelines and protocols for animal experimentation at Nathan S. Kline Institute.

Analysis of autolysosome acidity of TRGL mouse and Vesicle quantification

Immunohistochemistry was performed as previously described (Lee *et al.*, 2010). Animals were anesthetized with a mixture of ketamine 100 mg/kg body weight) and xylazine (10 mg/kg body weight) and intracardially perfused by 0.9% saline. Brains were dissected and immersed in the same fixative for 24 h and then 40-um sagittal sections were made using a vibratome. Immediately after sectioning, sections were immunolabeled with the indicated antibodies overnight and then visualized with Alexa Fluor conjugated secondary antibodies. Imaging was performed using a plan-Apochromat 40x/1.4 oil objective lens on a LSM880 laser scanning confocal microscope. The 3 colors (RGB; red, green, blue) intensity of each vesicle were calculated by Zen from Carl Zeiss Microscopy using the profile function. The R, G, and B ratio of each vesicle was calculated into a hue angle and saturation range by following formula: Hue° = IF(180/PI()*ATAN2(2*R-G-B,SQRT(3)*(G-B))<0,180/PI()*ATAN2(2*R-G-B,SQRT(3)*(G-B)) + 360,180/PI()*ATAN2(2*R-G-B,SQRT (3)* (G-B))). Saturation percent of the hue angle was calculated by entering the values of R, G, and B for a given puncta into the following formula = (MAX(RGB)-MIN(RGB))/SUM(MAX(RGB)+MIN(RGB))*100, provided lightness is less than 1, which is the usual case for our data. Vesicle quantification was performed as previously described (Lee *et al.*, 2019).

Saracatinib pharmacokinetics

To examine the effect of Fyn kinase inhibitor (Saracatinib) in a preclinical DS mouse model, mice received a dose of 5 mg/kg per day administered orally twice daily for 3-4 weeks

Lysosomal pH measurement

Procedures were performed as previously described (Wolfe et al., 2013). Following the addition of 250 μg LysoSensor™ Yellow/Blue dextran treatments, cells were incubated for 24 hr. The samples were then read in a Wallac Victor 2 fluorimeter (Perkin Elmer) with excitation at 355 nm. The ratio of emission 440 nm/535 nm was then calculated for each sample. The pH values were determined from the standard curve generated via pH calibration samples.

Lysosomal isolation

Cells were incubated in growth medium containing 10 % Dextran conjugated magnetite (DexoMAG™ 40) for 24 hr, then chased in normal growth media for 24 hr. Cells were washed with 1X PBS then harvested in 4 ml of ice-cold Buffer A (1 mM HEPES, pH 7.2, 15 mM KCl, 1.5 mM MgAc, 1 mM DTT, and 1X PIC). Cells were then homogenized with 40 strokes of a loose-fitting pestle in a Dounce homogenizer then passed through a 23 G needle 5 times. After homogenization, 500 μl of ice-cold Buffer B (220 mM HEPES, pH 7.2, 375 mM KCl, 22.5 mM MgAc, 1 mM DTT, and 20 μM DNase I) was added and samples were then centrifuged at 750 xg for 10 min. The supernatant was then decanted over a QuadroMACS™

LS column (Miltenyi Biotec, 130-042-976) that had previously been equilibrated with 0.5 % BSA in PBS, and then collected non-lysosomal fraction (Flow) to flow through via gravity. The pellet was subjected to re-addition of 4 ml ice cold Buffer A, 500 µl ice cold Buffer B and then re-suspended and re-centrifuged. This second supernatant was also passed over the column and allowed to flow through via gravity. DNase I (10 µl/ml in PBS) was added and the column was then incubated for 10 min and the washed with 1 ml ice cold PBS. Lysosomes were eluted by removing the column from the magnetic assembly, adding 100 µl of PBS for immunoblotting / M1 buffer (10 mM Tris, pH 7.5, 250 mM Sucrose, 150 mM KCl, 3 mM β-mercaptoethanol, and 20 mM $CaCl_2$) for v-ATPase activity and Proton Translocation assay and forced through the column using a plunger.

v-ATPase activity assay

Lysosome-enriched fractions (fibroblasts: 4 µg; mouse brain: mixture of 20 µl each Optiprep fraction from 15-18) were mixed with 0.052% NaN_3, which is an inhibitor of P- and F-type ATPase, to minimize nonspecific ATPase activity. The v-ATPase activity measured using ATPase assay kit according to the manufacturer's protocol. Control samples were measured in the presence of the v-ATPase inhibitor ConA (1 µM) and the experimental values were subtracted accordingly. Absorbance was measured at 650 nm and solutions of P_i were used to generate a standard curve.

Proton translocation assay

Proton transport activity into the lumen of isolated lysosomes was measured by fluorescence quenching of 9-amino-6-chloro-2-methoxyacridine (ACMA) in the presence or absence of 1 µM ConA. Lysosome-enriched fractions (25 µg) were added to a cuvette containing 2ml of reaction buffer (10 mM BisTrisPropene [BTP]-MES, pH 7.0, 25 mM KCl, 2 mM $MgSO_4$, 10 % glycerol and 2 µM ACMA). The reaction was started by the addition of 1 mM ATP in BTP, pH 7.5, a measurement (Ex412/Em480) taken every 5 sec for 600 sec on a SpectraMax M5 multimode reader (Molecular Devices).

Subcellular fractionation

For fibroblasts, cells were washed and harvested with 1X PBS then re-suspended in ice cold membrane preparation buffer (5 mM Tris, pH 7.4, 250 mM Sucrose, 1 mM EGTA, and 1X PIC). Cells were then briefly homogenized then passed through 26 G needle 10 times. For mouse brain, half of an adult mouse brain was homogenized in 10x volume homogenization buffer (HB: 250 mM sucrose, 10 mM Tris-HCl, pH 7.4, 1 mM EDTA, and protease and phosphatase inhibitors) by 40 strokes in a Teflon-coated pestle. After 10 min on ice, samples were then centrifuged at 1,000 xg for 10 min. The supernatants were fractionated into cytosolic and membrane fractions by high-speed centrifugation at 150,000 xg for 60 min. The membrane fractions (pellet after centrifugation) lysis with 100 µl lysis buffer (10 mM Tris, pH 7.4, 150 mM NaCl, 1 mM EDTA, 1 mM EGTA, 1 % Triton X-100, 0.5 % NP-40) and sonication for immunoblotting

Iodixanol step gradient

Half of an adult mouse brain was homogenized in 10x volume HB by 40 strokes in a Teflon-coated pestle. Lysates were centrifuged at 1,000 xg for 20 min to generate the post nuclear supernatant (PNS). The PNS was then adjusted to 25% OptiPrep with 50% OptiPrep in HB. The resulting mixture, 2 ml in 25% OptiPrep, was placed at the bottom of a clear ultracentrifuge tube and was overlaid successively with 1.5 ml each of 20, 15, 14, 12.5, 10, and 5% OptiPrep in cold HB. The gradients were centrifuged for 18 h at 100,000 xg at 4 °C in a SW 40 rotor (Beckman Coulter). 500 µl fractions were collected from the top of the ultracentrifuge tubes and analyzed by WB analysis.

Gel electrophoresis and immunoblotting

Samples were mixed with 2X urea sample buffer (9.6 % SDS, 4M Urea, 16% Sucrose, 0.005% Bromophenol blue [BPB], and 4.6% β-mercaptoethanol) and incubated 15 min at 55 ºC for V0 subunits of v-ATPase electrophoresis, otherwise samples mixed with 1X SDS sample buffer (62.5 mM Tris, pH 6.8, 10 % Glycerol, 1 % SDS, 20 mM DTT, 5% β-mercaptoethanol, and 0.005 % BPB) and incubated 5 min at 100 ºC followed by electrophoresis on Novex™ 4-20% Tris-Glycine gradient gels (Invitrogen, WXP42020BOX; WXP42026BOX). Proteins were transferred onto 0.2 µm nitrocellulose membranes (Pall

Laboratory, p/n 66485) and the membrane was blocked using 5% non-fat milk or 5% BSA for detecting phospho-proteins. The membrane was then incubated overnight in primary antibody followed by incubation with HRP conjugated secondary antibody. The blot was developed using ECL-kits.

Immunoprecipitation (IP)

Proteins were prepared from cells using ULTRARIPA® kit for Lipid Raft according to the manufacturer's protocol. 1 mg of cell lysates were pulled down with proper antibodies for 24 hr at 4 ºC with gentle rotation. The mixture was then incubated with 30 µl of Protein A/G Mix Magnetic Beads and washed with lysis buffer and Magnetic Stand. The samples were dissociated by 2X Urea sample buffer.

Native gel immunoblot analysis

The pellet from the cell membrane fraction was resolved with 1% Digitonin and 1X NativePAGE™ sample buffer, incubated on ice for 30 min, and then centrifuged at 20,000 xg for 30 min. 15 µg of sample was mixed with 1 % NativePAGE™ G-250 sample additive followed by electrophoresis on NativePAGE™ Novex® 4-16% Bis-Tris Gels in 1X NativePAGE™ Running Buffer then transfer using 1X NuPAGE® Transfer buffer and 0.45 µm PVDF membranes (Millipore, IPVH00010) according to manufacturer's protocol.

Confocal fluorescence microscopy

Cells were fixed with 4 % PFA for 20 min, blocked with 5 % horse serum, incubated with anti-cathepsin B goat pAb (CTSB; 1/250) for lysosomal marker and anti-V1D rabbit mAb (1/100) overnight at 4 ºC, followed by fluorescence tagged secondary antibodies; Donkey anti-Goat Alexa Fluor 488 (1/500) and goat anti-Rabbit Alexa Fluor 568 (1/500). Cells were imaged using a plan-Apochromat 40x/1.4 oil DIC objective lens on the laser scanning confocal microscope, LSM 510 META, with LSM software v3.5 (Carl Zeiss MicroImage Inc). Images were analyzed using ImageJ program (NIH). Co-localization was determined using the Coloc 2 analysis tool on ImageJ software.

Proximity ligation assay

Proximity ligation assays were performed according to the manufacturer's protocol using the following reagents in the Duolink® In Situ Detection Reagents Red kit. In brief, cells were plated on cover slips at a concentration of 10^5/ml. Cells were fixed using 4 % PFA in PBS for 15 min, then permeabilized using 0.01 % Triton in PBS for 20 min at room temperature. All subsequent incubations were performed at 37 ºC in a humid chamber. Non-specific binding was minimized with the manufacturer's blocking buffer for 30 min. Cells were incubated with primary anti-APP (C1/6.1) mouse (1/100) and anti-V0a1 rabbit mAb (1/100) overnight at 4 ºC and washed with buffer A (twice, 5 min). Coverslips were incubated with ligation mix for 30 min, washed twice with buffer A, and incubated with amplification mix. Coverslips were then washed with provided Buffer B twice (10 min), followed by 1 min washing with 0.01x Wash Buffer B. The samples were mounted with Duolink® In Situ Mounting Medium with DAPI in the dark for 15 min at room temperature. The images were taken using a Zeiss LSM880 laser scanning confocal microscope at 20x objective lens. The number of signals per cell were analyzed using ImageJ program and then normalized to the protein levels.

RNA sequencing (RNA-seq) and data analysis

Procedures were performed as previously described (Jiang *et al.*, 2019).

Mass spectrometry (MS) analysis

The stained protein gel regions (Fig. S1B, Bands 1-6) were excised, and in-gel digestion was performed overnight with mass spectrometry grade Trypsin at 5 ng/µl in 50 mM NH_4HCO_3 digest buffer. After acidification with 10 % formic acid, peptides were extracted with 5 % formic acid/50 % acetonitrile (v/v) and concentrated to a small droplet using vacuum centrifugation. Desalting of peptides was done using hand packed SPE Empore C18 Extraction Disks (aka Stage Tips, 3M. St. Paul, MN, USA) as described (Rappsilber et al., 2007). Desalted peptides were again concentrated and reconstituted in 10 µl 0.1 % formic acid in water. An aliquot of the peptides was analyzed by nano-LC-MS/MS using an Easy nLC 1,000 equipped with a self-packed 75 µm x 20 cm reverse phase column (ReproSil-Pur C18, 3 m, Dr.

Maisch GmbH, Germany) coupled online to QExactive HF Orbitrap mass spectrometer via a Nanospray Flex source (all instruments from Thermo Scienctific, Waltham, MA, USA). Analytical column temperature was maintained at 50 ºC by a column oven (Sonation GmBH, Germany). Peptides were eluted with a 3-40% acetonitrile gradient over 60 min at a flow rate of 250 nl/min. The mass spectrometer was operated in the DDA mode with survey scans acquired at a resolution of 120,000 (at m/z 200) over a scan range of 300-1,750 m/z. Up to 15 of the most fragmentation by higher-energy collisional dissociation with a normalized collision energy of 27. The maximum injection times for the survey and MS/MS scans were 60 ms. And the ion target value for both scan modes was set to 3e6. All acquired mass spectra were first converted to mascot generic format files (mgf) using Proteome Discoverer 1.4 and generated mgf files searched against a human protein database (SwissProt, 20, 210 sequences, 2014) using Mascot (Matrix Science, London, UK; version 2.7.0 www.matrixscience.com). Decoy proteins are added to the search to allow for the calculation of false discovery rates (FDR). The search parameters are as follows: (i) two missed cleavage tryptic sites are allowed; (ii) precursor ion mass tolerance = 10 ppm; (iii) fragment ion mass tolerance = 0.3 Da; and (iv) variable protein modifications are allowed for methionine oxidation, deamidation of asparagine and glutamines, cysteine acrylamide derivatization and protein N-terminal acetylation. MudPit scoring is typically applied using significance threshold score $p<0.01$. Decoy database search is always activated and, in general, for merged LS-MS/MS analysis of a gel lane with $p<0.01$, false discovery rate for protein ID averaged around 1 %.

Protein preparation for Glide molecular docking

The cryo-EM structure of the v-ATPase was retrieved from the Protein Data Bank (PDB ID: 6VQ7), and it was refined with Protein Preparation Wizard implemented in Maestro 12. The protein structure was imported into workspace and preprocessed to assign bond orders, add hydrogen atoms, create zero-order bonds to metals, create disulfide bonds, and to delete water molecules beyond 5 Å from hetero groups. In addition, missing atoms in residues and missing loops were added using Prime to generate a complete protein structure (note: the 34 missing amino acids (R133 – G169) in the V0a1 subunit was not built using Prime due to the size of the missing loop). The protein structure was further refined via automated H-bond assignment and restrained minimization with OPLS 2005 force field by converging heavy atoms to 0.3 Å RMSD. The N-terminal domain of the V0a1 subunit (E2 – Y363) was retrieved by deleting other subunits. The missing loop (R133 – G169) was built using the 3D builder module in Maestro 12, and the complete N-terminal domain of the V0a1 subunit was further refined with Protein Preparation Wizard. The folding states of the missing loop were searched by MD simulation using the Amber Molecular Dynamics Package. The truncated protein structure (N111 – V271) with ACE and NME terminal caps was solvated with the Amber ff14SB force field and TIP3P explicit water model in an octahedron periodic box using a buffer distance of 14.0 Å containing 150 mM NaCl in 20,827 water molecules. The solvated protein structure was treated to 3 consecutive minimization stages: (1) 1,000 steps of steepest descent and 1,000 steps of conjugate gradient minimization with 100 kcal mol^{-1} $Å^{-2}$ restraints on all atoms except water molecules; (2) 2,500 steps of steepest descent and 2,500 steps of conjugate gradient minimization without restraints; and (3) 1,000 steps of steepest descent and 2,500 steps of conjugate minimization with 100 kcal mol^{-1} $Å^{-2}$ restraints on N111 – F130 and Q252 – V271, which are helix units connected to the rest of the V0a1 subunit. After minimization, equilibration of the solvated protein was performed at 303.15 K for 100 ns under constant volume, with a timestep of 2 fs, and with SHAKE algorithm employed to restrain on calculation of forces of bonds containing hydrogen atoms. In the equilibration, amide backbones of N112 – K129 and F170 – V271 were fixed with 10 kcal mol^{-1} $Å^{-2}$ restraints. The last frame of the MD equilibration was extracted from the simulation trajectories using the CPPTRAJ program in the AmberTools20, and it was subjected to the Glide docking after removing water molecules and ions.

Glide molecular docking and MD simulations

The last frame of the MD simulation was refined by Protein Preparation Wizard, and a protein grid for Glide dock was generated. Van der Waals radius was scaled by decreasing the default value of scaling factor to 0.8 to soften the potential for nonpolar parts of the receptor. The length of the inner box was increased to 20 $Å^3$ from the default value (10 $Å^3$) to explore all available binding sites of the target protein in the molecular docking. A ligand structure (NGpYEN) was built using the 3D build module and the N- and C-terminal amino acids were capped with the acetyl group (ACE) and N-methylamine (NMA) in the refinement step, respectively. Glide software (v 8.7) in Maestro 12 was utilized to dock the ligand

structure to the protein grid in the standard precision mode with the OPLS 2005 force field. The ligand structure was flexibly docked by sampling rotatable bonds, nitrogen inversions, and ring conformations. For the output of Glide docking, 200 poses were included for post-docking minimization, and 95 binding poses of the NGpYEN structure were obtained. After visual analysis by considering docking scores, 16 diverse binding poses of the NGpYEN structure at multiple binding sites were selected for further modeling with molecular dynamics. Each complex structure of the truncated V0a1 with each binding pose of NGpYEN was solvated with TIP3P explicit water model in an octahedron periodic box using a buffer distance of 14.0 Å containing 150 mM NaCl in ca. 13,000 water molecules. Amber ff14SB and phosaa14SB force fields were applied to the solvated protein – ligand complex for MD simulation. Minimization and equilibration of the solvated protein – ligand complexes were conducted for 10 ns with the same parameters and constraints aforementioned. The last frame of the equilibration was obtained from the trajectories, and additional amino acids were added to the ligand structure in Maestro 12. Multiple minimization and equilibration were iteratively conducted for 480 ns with the same parameters and various constraints. VMD software was used to visually analyze the trajectories, and the binding pose of the ligand that showed similar binding pattern to the known structure of pY to its pocket (Fig. SS1) was selected. Figures were generated using Pymol (The PyMOL Molecular Graphics System, Version 2.0 Schrodinger, LLC).

Estimation of Binding Affinity using MM-GBSA.

The binding free energies of the V0a1 model structure in complex with phosphorylated and unphosphorylated ligands were estimated by generalized Born surface area continuum solvation method (MM-GBSA). The truncated V0a1 – a phosphorylated ligand (ACE-MQQNGpYENPTYK-NMA) structure was obtained from the previous restricted MD simulation followed by protein preparation in Maestro 12. The model structure without the phosphorylated Y was obtained by mutating pY to Y in Maestro 12. These model structures were solvated as described above, and the whole systems were minimized by 2,500 steps of steepest descent and 2,500 steps of conjugate gradient minimization without restraints. After minimization, the systems were heated from 0 K to 303.15 K for 300 ps and equilibrated for 100 ps under NVT condition followed by another equilibration for 100 ps under NPT condition. Finally, 10 ns production run for each system was executed at a constant pressure (1 bar) and a constant temperature (303.15 K). The estimated binding free energy of each system was calculated with all trajectories (1,000 frames) of the complexes.

QUANTIFICATION AND STATISTICAL ANALYSIS

All quantitative data were subjected to two-tailed unpaired Student's *t*-test for single comparison, or one-way ANOVA analysis for multiple comparisons with Sidak's analysis using GraphPad Prism 8. For data more than 3 repeat, mean ± SEM were represented in bar graph. Statistically significance is represented with asterisks or hatch marks * or $^{\#}$, $p \leq 0.05$; ** or $^{\#\#}$, $p \leq 0.005$; *** or $^{\#\#\#}$, $p \leq 0.0005$; **** or $^{\#\#\#\#}$, $p \leq 0.0001$.

SUPPLEMENTAL INFORMATION

Supplementary Figure S1. Related to Figure 1

(A) The immunoblot represents purity of lysosomal enriched fraction. (B) *Left panel:* Membrane fractions were resolved using the native PAGE and immunoblotted with anti-V1B2 antibody. The light version is same blot as in Fig. 1E, and the dark version is longer exposal blot of Fig. 1E. *Right panel:* Membrane fractions were resolved using native PAGE and fixed with fix solution (40% methanol, 10% acetic acid). The fixed gel stained with Coomassie R-250 Stain (0.02% Coomassie R-250 in 30% methanol and 10% acetic acid) and then destained with destaining solution (8% acetic acid). (C) The table represents total mass spectrometry spectral counts of each band to indicate relative abundance of the v-ATPase subunits.

Supplementary Figure S2. Related to Figure 1

(A) Lysosomal pH values measured ratiometrically using LysoSensor Yellow/Blue (Y/B) dextran using lysosome enrichment fraction from 5 months fibroblasts. (B) Lysosomal v-ATPase activity measured colorimetrically as ATP hydrolysis with and without a v-ATPase inhibitor (Concanamycin A; ConA). Activity assay is performed on lysosomal fractions pre-treated with inhibitors of P- and F-type ATPases (*o*-vanadate) to minimize nonspecific ATPase activity using 5 months fibroblasts. (C and D) Lysosomal v-ATPase activity measured fluorometrically using a pH gradient probe (ACMA method) to measure H^+ transport into lysosomes by the v-ATPase with and without a ConA using 5 mon fibroblasts. (E) Membrane fractions from 5 months fibroblasts were resolved using native PAGE and immunoblotted with anti-V1B2 antibody. (F) The graph represents ratio of full complex versus total (full plus sub complexes) complexes of v-ATPase. (G) Immunoblot of v-ATPase subunit distributions in total lysates (Total) and lysosomal enriched (Lyso.) fraction of 5 months 2N and DS fibroblasts. LAMP1 served as a marker for lysosome and Actin served as a loading control for total lysates. (H) The graphs show band intensity of each v-ATPase subunits.

Supplementary Figure S3. Related to Figure 3

(A-C) The immunoblot represents CTFs and flAPP protein levels in total lysates from 2N and DS fibroblast after treated with either DMSO (-), γ-Sec INH (10 μM) (*A*), BACE INH (10 μM) (*B*), or α-Sec INH (20 μM) (*C*), for 24 hr. Actin and GAPDH served as a loading control. (D)

Lysosomal pH of 2N and DS fibroblasts treated with either DMSO (No Tx) or α-secretase inhibitor, TAPI-1 (α-Sec INH; 20 μM), for 24 hr determined by LysoSensor Y/B dextran. (E) Lysosomal v-ATPase activity measured colorimetrically as ATP hydrolysis with and without a ConA. Activity assay performed on lysosomal fractions from 2N and DS fibroblast after treated with DMSO or 20 μM α-Sec INH for 24 hr, pre-treated with *o*-vanadate to minimize nonspecific ATPase activity. (F) Membrane fractions from 2N and DS fibroblasts treated with DMSO (-) or α-Sec INH (+) were resolved using the native PAGE and immunoblotted with anti-V1B2 antibody. (G) The graph represents ratio of full complex versus total (full plus partial complexes) complexes of v-ATPase.

Supplementary Figure S4. Related to Figure 4

(A) Cell lysates were incubated with $A\beta_{1-42}$ peptide following indicated amount for 24 hr, then immunoprecipitated with anti-APP (C1/6.1) antibody, followed by immunoblotting with anti-V0a1 antibody. The values at the bottom of the left IP blot indicate the relative intensities of IP-ed V0a1normalized by IP-ed APP-CTFs. (B) Lysosomal pH of 2N and DS fibroblasts treated with either DMSO (-) or 5 μM $A\beta_{1-42}$ peptide for 24 hr determined by LysoSensor Y/B dextran. (C) A known binding site of phosphorylated tyrosine residue (X-ray co-crystal structure of Grb2-SH2 (gray) and AICD (green) complex, PDB ID: 3MXC). The phosphate unit shows hydrogen bond and salt bridge interactions as presented with yellow dashed lines. The phenyl ring of tyrosine form π – hydrophobic contacts with the methylene unit of K109. (D) The cryo-EM structure of V0a1 subunit of v-ATPase (PDB ID: 6VQ7) and the unsolved loop. An unsolved loop in the cryo-EM structure is built by using maestro molecular modeling software (green), and three consecutive serine residues (red box) in the unsolved loop are labeled. (E) Multiple sequence alignment of the unsolved loop of V0a1 subunits shows that three serine residues (red box) are highly conserved among species. The first column shows UniProt entry code, and VPP1_HUMAN, RAT, BOVIN, MOUSE, XENTR, CHICK, PONAB, XENLA, and CAEEL represent human, rat, bovine, mouse, frog, chicken, orangutan, C. elegans v-ATPase V0a1 subunits, respectively.

Supplementary Figure S5. Related to Figure 5

(A) Immunoblot represents phospho-Fyn (pFyn) and Fyn kinase protein levels in 2N and DS fibroblast after treated with DMSO (-) or Fyn inhibitor following indicated amount for 24 hr. (B) Immunoblot represents Fyn kinase protein levels in 2N and DS fibroblast after transfected without (-) or with siNC or siFyn following indicated amount for 48 hr.

Supplementary Figure S6. Related to Figure 6

Adult mouse brain homogenates were fractionated through an iodixanol step gradient. Immunoblot analysis showed the distribution of cathepsin B (CTSB; lysosome marker; Ly), Rab5 (early endosome marker; EE), Rab7 (late endosome marker; LE), syntaxin 6 (STX6; trans-golgi network marker; TGN), PDI (endoplasmic reticulum marker; ER), and Tubulin (Cytosolic marker; Cyto). Red box indicates lysosomal enriched fraction (15~18).

Supplementary Figure S7.

(A) Lysosomal v-ATPase activity measured colorimetrically as ATP hydrolysis with and without ConA. Activity assays were performed on lysosomal enriched fraction (15-18) of iodixanol step gradient from 6-months Tg2576 female adult brain pre-treated with *o*-vanadate to minimize nonspecific ATPase activity. (B) Immunoblot represents phospho-APP (pY^{682}CTFs and pY^{682}flAPP), APP (CTFs and flAPP), phospho-Y^{420}Fyn and Fyn kinase protein levels in 6-months female Tg2576. (C) The graph shows band intensity of pY^{682}CTF (pCTF), pY^{682}flAPP (pflAPP), and pY^{420}Fyn (pFyn) proteins. (D and E) The graph show correlation between protein levels of pY^{420}Fyn and pY^{682}CTF (circle) (*D*) or pY^{682}flAPP (diamond) (*E*). Blue represents band intensity of phospho-Tyr proteins from control (WT) mice and red represents band intensity of phospho-Tyr proteins from Tg2576 mice. R-squared values displayed on charts. (F) Lysosomal v-ATPase activity measured colorimetrically as ATP hydrolysis with and without ConA. Activity assays were performed on lysosomal enriched fraction (15-18) of iodixanol step gradient from 6-months 5xFAD female adult brain pre-treated with *o*-vanadate to minimize nonspecific ATPase activity. (G) Immunoblot represents phospho-APP (pY^{682}CTFs and pY^{682}flAPP), APP (CTFs and flAPP), phospho-Y^{420}Fyn and Fyn kinase protein levels in 6-months female 5xFAD. (H) The graphs show band intensity of pY^{682}CTF (pCTF), pY^{682}flAPP (pflAPP), and pY^{420}Fyn (pFyn) proteins. (I and J) The graph show correlation between protein levels of pY^{420}Fyn and pY^{682}CTF (circle) (*I*) or pY^{682}flAPP (diamond) (*J*). Blue represents band

intensity of phospho-Tyr proteins from control (WT) mice and red represents band intensity of phospho-Tyr proteins from 5xFAD mice. R-squared values displayed on charts.

REFERENCES

Abbas, Y.M., Wu, D., Bueler, S.A., Robinson, C.V., and Rubinstein, J.L. (2020). Structure of V-ATPase from the mammalian brain. Science *367*, 1240-1246. 10.1126/science.aaz2924.

Almeida, M.F., Bahr, B.A., and Kinsey, S.T. (2020). Endosomal-lysosomal dysfunction in metabolic diseases and Alzheimer's disease. International review of neurobiology *154*, 303-324. 10.1016/bs.irn.2020.02.012.

Ando, K., Iijima, K.I., Elliott, J.I., Kirino, Y., and Suzuki, T. (2001). Phosphorylation-dependent regulation of the interaction of amyloid precursor protein with Fe65 affects the production of beta-amyloid. J Biol Chem *276*, 40353-40361. 10.1074/jbc.M104059200.

Ballabio, A., and Bonifacino, J.S. (2020). Lysosomes as dynamic regulators of cell and organismal homeostasis. Nat Rev Mol Cell Biol *21*, 101-118. 10.1038/s41580-019-0185-4.

Boland, B., Yu, W.H., Corti, O., Mollereau, B., Henriques, A., Bezard, E., Pastores, G.M., Rubinsztein, D.C., Nixon, R.A., Duchen, M.R., et al. (2018). Promoting the clearance of neurotoxic proteins in neurodegenerative disorders of ageing. Nature reviews. Drug discovery *17*, 660-688. 10.1038/nrd.2018.109.

Bordi, M., Berg, M.J., Mohan, P.S., Peterhoff, C.M., Alldred, M.J., Che, S., Ginsberg, S.D., and Nixon, R.A. (2016). Autophagy flux in CA1 neurons of Alzheimer hippocampus: Increased induction overburdens failing lysosomes to propel neuritic dystrophy. Autophagy *12*, 2467-2483. 10.1080/15548627.2016.1239003.

Brouillard, M., Barthélémy, P., Dehay, B., Crauste-Manciet, S., and Desvergnes, V. (2021). Nucleolipid Acid-Based Nanocarriers Restore Neuronal Lysosomal Acidification Defects. Frontiers in chemistry *9*, 736554. 10.3389/fchem.2021.736554.

Butterfield, D.A., Di Domenico, F., Swomley, A.M., Head, E., and Perluigi, M. (2014). Redox proteomics analysis to decipher the neurobiology of Alzheimer-like neurodegeneration: overlaps in Down's syndrome and Alzheimer's disease brain. The Biochemical journal *463*, 177-189. 10.1042/bj20140772.

Case, D.A., Cheatham, T.E., 3rd, Darden, T., Gohlke, H., Luo, R., Merz, K.M., Jr., Onufriev, A., Simmerling, C., Wang, B., and Woods, R.J. (2005). The Amber biomolecular simulation programs. Journal of computational chemistry *26*, 1668-1688. 10.1002/jcc.20290.

Cataldo, A.M., Hamilton, D.J., Barnett, J.L., Paskevich, P.A., and Nixon, R.A. (1996). Properties of the endosomal-lysosomal system in the human central nervous system: disturbances mark most neurons in populations at risk to degenerate in Alzheimer's disease. J Neurosci *16*, 186-199. 10.1523/jneurosci.16-01-00186.1996.

Cataldo, A.M., Mathews, P.M., Boiteau, A.B., Hassinger, L.C., Peterhoff, C.M., Jiang, Y., Mullaney, K., Neve, R.L., Gruenberg, J., and Nixon, R.A. (2008). Down syndrome fibroblast model of Alzheimer-related endosome pathology: accelerated endocytosis promotes late endocytic defects. Am J Pathol *173*, 370-384. 10.2353/ajpath.2008.071053.

Cataldo, A.M., Peterhoff, C.M., Schmidt, S.D., Terio, N.B., Duff, K., Beard, M., Mathews, P.M., and Nixon, R.A. (2004). Presenilin mutations in familial Alzheimer disease and transgenic mouse models accelerate neuronal lysosomal pathology. J Neuropathol Exp Neurol *63*, 821-830. 10.1093/jnen/63.8.821.

Česen, M.H., Pegan, K., Spes, A., and Turk, B. (2012). Lysosomal pathways to cell death and their therapeutic applications. Experimental cell research *318*, 1245-1251. 10.1016/j.yexcr.2012.03.005.

Checler, F., Afram, E., Pardossi-Piquard, R., and Lauritzen, I. (2021). Is γ-secretase a beneficial inactivating enzyme of the toxic APP C-terminal fragment C99? J Biol Chem *296*, 100489. 10.1016/j.jbc.2021.100489.
Colacurcio, D.J., and Nixon, R.A. (2016). Disorders of lysosomal acidification-The emerging role of v-ATPase in aging and neurodegenerative disease. Ageing Res Rev *32*, 75-88. 10.1016/j.arr.2016.05.004.
Colacurcio, D.J., Pensalfini, A., Jiang, Y., and Nixon, R.A. (2018). Dysfunction of autophagy and endosomal-lysosomal pathways: Roles in pathogenesis of Down syndrome and Alzheimer's Disease. Free Radic Biol Med *114*, 40-51. 10.1016/j.freeradbiomed.2017.10.001.
Cotter, K., Stransky, L., McGuire, C., and Forgac, M. (2015). Recent Insights into the Structure, Regulation, and Function of the V-ATPases. Trends Biochem Sci *40*, 611-622. 10.1016/j.tibs.2015.08.005.
Das, S., Raychaudhuri, M., Sen, U., and Mukhopadhyay, D. (2011). Functional implications of the conformational switch in AICD peptide upon binding to Grb2-SH2 domain. J Mol Biol *414*, 217-230. 10.1016/j.jmb.2011.09.046.
De Jonghe, C., Esselens, C., Kumar-Singh, S., Craessaerts, K., Serneels, S., Checler, F., Annaert, W., Van Broeckhoven, C., and De Strooper, B. (2001). Pathogenic APP mutations near the gamma-secretase cleavage site differentially affect Abeta secretion and APP C-terminal fragment stability. Hum Mol Genet *10*, 1665-1671. 10.1093/hmg/10.16.1665.
De Strooper, B. (2007). Loss-of-function presenilin mutations in Alzheimer disease. Talking Point on the role of presenilin mutations in Alzheimer disease. EMBO Rep *8*, 141-146. 10.1038/sj.embor.7400897.
Del Prete, D., Lombino, F., Liu, X., and D'Adamio, L. (2014). APP is cleaved by Bace1 in pre-synaptic vesicles and establishes a pre-synaptic interactome, via its intracellular domain, with molecular complexes that regulate pre-synaptic vesicles functions. PLoS One *9*, e108576. 10.1371/journal.pone.0108576.
Diwu, Z., Chen, C.S., Zhang, C., Klaubert, D.H., and Haugland, R.P. (1999). A novel acidotropic pH indicator and its potential application in labeling acidic organelles of live cells. Chem Biol *6*, 411-418. 10.1016/s1074-5521(99)80059-3.
Doran, E., Keator, D., Head, E., Phelan, M.J., Kim, R., Totoiu, M., Barrio, J.R., Small, G.W., Potkin, S.G., and Lott, I.T. (2017). Down Syndrome, Partial Trisomy 21, and Absence of Alzheimer's Disease: The Role of APP. J Alzheimers Dis *56*, 459-470. 10.3233/jad-160836.
Forgac, M. (2007). Vacuolar ATPases: rotary proton pumps in physiology and pathophysiology. Nat Rev Mol Cell Biol *8*, 917-929. 10.1038/nrm2272.
Guenette, S., Strecker, P., and Kins, S. (2017). APP Protein Family Signaling at the Synapse: Insights from Intracellular APP-Binding Proteins. Front Mol Neurosci *10*, 87. 10.3389/fnmol.2017.00087.
Halgren, T.A., Murphy, R.B., Friesner, R.A., Beard, H.S., Frye, L.L., Pollard, W.T., and Banks, J.L. (2004). Glide: a new approach for rapid, accurate docking and scoring. 2. Enrichment factors in database screening. Journal of medicinal chemistry *47*, 1750-1759. 10.1021/jm030644s.
Ho, G.J., Hashimoto, M., Adame, A., Izu, M., Alford, M.F., Thal, L.J., Hansen, L.A., and Masliah, E. (2005). Altered p59Fyn kinase expression accompanies disease progression in Alzheimer's disease: implications for its functional role. Neurobiol Aging *26*, 625-635. 10.1016/j.neurobiolaging.2004.06.016.

Hoe, H.S., Minami, S.S., Makarova, A., Lee, J., Hyman, B.T., Matsuoka, Y., and Rebeck, G.W. (2008). Fyn modulation of Dab1 effects on amyloid precursor protein and ApoE receptor 2 processing. J Biol Chem *283*, 6288-6299. 10.1074/jbc.M704140200.
Hoey, S.E., Williams, R.J., and Perkinton, M.S. (2009). Synaptic NMDA receptor activation stimulates alpha-secretase amyloid precursor protein processing and inhibits amyloid-beta production. J Neurosci *29*, 4442-4460. 10.1523/jneurosci.6017-08.2009.
Holsinger, R.M., McLean, C.A., Beyreuther, K., Masters, C.L., and Evin, G. (2002). Increased expression of the amyloid precursor beta-secretase in Alzheimer's disease. Annals of neurology *51*, 783-786. 10.1002/ana.10208.
Hsiao, K., Chapman, P., Nilsen, S., Eckman, C., Harigaya, Y., Younkin, S., Yang, F., and Cole, G. (1996). Correlative memory deficits, Abeta elevation, and amyloid plaques in transgenic mice. Science *274*, 99-102. 10.1126/science.274.5284.99.
Hwang, J., Estick, C.M., Ikonne, U.S., Butler, D., Pait, M.C., Elliott, L.H., Ruiz, S., Smith, K., Rentschler, K.M., Mundell, C., et al. (2019). The Role of Lysosomes in a Broad Disease-Modifying Approach Evaluated across Transgenic Mouse Models of Alzheimer's Disease and Parkinson's Disease and Models of Mild Cognitive Impairment. International journal of molecular sciences *20*. 10.3390/ijms20184432.
Iannuzzi, F., Sirabella, R., Canu, N., Maier, T.J., Annunziato, L., and Matrone, C. (2020). Fyn Tyrosine Kinase Elicits Amyloid Precursor Protein Tyr682 Phosphorylation in Neurons from Alzheimer's Disease Patients. Cells *9*. 10.3390/cells9081807.
Jiang, Y., Mullaney, K.A., Peterhoff, C.M., Che, S., Schmidt, S.D., Boyer-Boiteau, A., Ginsberg, S.D., Cataldo, A.M., Mathews, P.M., and Nixon, R.A. (2010). Alzheimer's-related endosome dysfunction in Down syndrome is Abeta-independent but requires APP and is reversed by BACE-1 inhibition. Proc Natl Acad Sci U S A *107*, 1630-1635. 10.1073/pnas.0908953107.
Jiang, Y., Sato, Y., Im, E., Berg, M., Bordi, M., Darji, S., Kumar, A., Mohan, P.S., Bandyopadhyay, U., Diaz, A., et al. (2019). Lysosomal Dysfunction in Down Syndrome Is APP-Dependent and Mediated by APP-betaCTF (C99). J Neurosci *39*, 5255-5268. 10.1523/jneurosci.0578-19.2019.
Kaufman, A.C., Salazar, S.V., Haas, L.T., Yang, J., Kostylev, M.A., Jeng, A.T., Robinson, S.A., Gunther, E.C., van Dyck, C.H., Nygaard, H.B., and Strittmatter, S.M. (2015). Fyn inhibition rescues established memory and synapse loss in Alzheimer mice. Annals of neurology *77*, 953-971. 10.1002/ana.24394.
Kim, S., Sato, Y., Mohan, P.S., Peterhoff, C., Pensalfini, A., Rigoglioso, A., Jiang, Y., and Nixon, R.A. (2016). Evidence that the rab5 effector APPL1 mediates APP-betaCTF-induced dysfunction of endosomes in Down syndrome and Alzheimer's disease. Mol Psychiatry *21*, 707-716. 10.1038/mp.2015.97.
Knopman, D.S., Amieva, H., Petersen, R.C., Chételat, G., Holtzman, D.M., Hyman, B.T., Nixon, R.A., and Jones, D.T. (2021). Alzheimer disease. Nature reviews. Disease primers *7*, 33. 10.1038/s41572-021-00269-y.
Kramer-Albers, E.M., and White, R. (2011). From axon-glial signalling to myelination: the integrating role of oligodendroglial Fyn kinase. Cell Mol Life Sci *68*, 2003-2012. 10.1007/s00018-010-0616-z.
Lauritzen, I., Pardossi-Piquard, R., Bourgeois, A., Pagnotta, S., Biferi, M.G., Barkats, M., Lacor, P., Klein, W., Bauer, C., and Checler, F. (2016). Intraneuronal aggregation of the β-CTF fragment of APP (C99) induces Aβ-independent lysosomal-autophagic pathology. Acta Neuropathol *132*, 257-276. 10.1007/s00401-016-1577-6.

Lee, J.H., McBrayer, M.K., Wolfe, D.M., Haslett, L.J., Kumar, A., Sato, Y., Lie, P.P., Mohan, P., Coffey, E.E., Kompella, U., et al. (2015). Presenilin 1 Maintains Lysosomal Ca(2+) Homeostasis via TRPML1 by Regulating vATPase-Mediated Lysosome Acidification. Cell Rep *12*, 1430-1444. 10.1016/j.celrep.2015.07.050.
Lee, J.H., Rao, M.V., Yang, D.S., Stavrides, P., Im, E., Pensalfini, A., Huo, C., Sarkar, P., Yoshimori, T., and Nixon, R.A. (2019). Transgenic expression of a ratiometric autophagy probe specifically in neurons enables the interrogation of brain autophagy in vivo. Autophagy *15*, 543-557. 10.1080/15548627.2018.1528812.
Lee, J.H., Wolfe, D.M., Darji, S., McBrayer, M.K., Colacurcio, D.J., Kumar, A., Stavrides, P., Mohan, P.S., and Nixon, R.A. (2020). β2-adrenergic Agonists Rescue Lysosome Acidification and Function in PSEN1 Deficiency by Reversing Defective ER-to-lysosome Delivery of ClC-7. J Mol Biol *432*, 2633-2650. 10.1016/j.jmb.2020.02.021.
Lee, J.H., Yu, W.H., Kumar, A., Lee, S., Mohan, P.S., Peterhoff, C.M., Wolfe, D.M., Martinez-Vicente, M., Massey, A.C., Sovak, G., et al. (2010). Lysosomal proteolysis and autophagy require presenilin 1 and are disrupted by Alzheimer-related PS1 mutations. Cell *141*, 1146-1158. 10.1016/j.cell.2010.05.008.
Li, R., Lindholm, K., Yang, L.B., Yue, X., Citron, M., Yan, R., Beach, T., Sue, L., Sabbagh, M., Cai, H., et al. (2004). Amyloid beta peptide load is correlated with increased beta-secretase activity in sporadic Alzheimer's disease patients. Proc Natl Acad Sci U S A *101*, 3632-3637. 10.1073/pnas.0205689101.
Liberman, R., Bond, S., Shainheit, M.G., Stadecker, M.J., and Forgac, M. (2014). Regulated assembly of vacuolar ATPase is increased during cluster disruption-induced maturation of dendritic cells through a phosphatidylinositol 3-kinase/mTOR-dependent pathway. J Biol Chem *289*, 1355-1363. 10.1074/jbc.M113.524561.
Lie, P.P.Y., and Nixon, R.A. (2019). Lysosome trafficking and signaling in health and neurodegenerative diseases. Neurobiology of disease *122*, 94-105. 10.1016/j.nbd.2018.05.015.
Lott, I.T., and Head, E. (2019). Dementia in Down syndrome: unique insights for Alzheimer disease research. Nat Rev Neurol *15*, 135-147. 10.1038/s41582-018-0132-6.
Luzio, J.P., Pryor, P.R., and Bright, N.A. (2007). Lysosomes: fusion and function. Nat Rev Mol Cell Biol *8*, 622-632. 10.1038/nrm2217.
Mindell, J.A. (2012). Lysosomal acidification mechanisms. Annu Rev Physiol *74*, 69-86. 10.1146/annurev-physiol-012110-142317.
Mortimore, G.E., and Schworer, C.M. (1977). Induction of autophagy by amino-acid deprivation in perfused rat liver. Nature *270*, 174-176. 10.1038/270174a0.
Nakamura, S. (2004). Glucose activates H(+)-ATPase in kidney epithelial cells. Am J Physiol Cell Physiol *287*, C97-105. 10.1152/ajpcell.00469.2003.
Nixon, R.A. (2007). Autophagy, amyloidogenesis and Alzheimer disease. J Cell Sci *120*, 4081-4091. 10.1242/jcs.019265.
Nixon, R.A. (2013). The role of autophagy in neurodegenerative disease. Nat Med *19*, 983-997. 10.1038/nm.3232.
Nixon, R.A. (2017). Amyloid precursor protein and endosomal-lysosomal dysfunction in Alzheimer's disease: inseparable partners in a multifactorial disease. Faseb j *31*, 2729-2743. 10.1096/fj.201700359.
Nixon, R.A. (2020). The aging lysosome: An essential catalyst for late-onset neurodegenerative diseases. Biochimica et biophysica acta. Proteins and proteomics *1868*, 140443. 10.1016/j.bbapap.2020.140443.

Nixon, R.A., and Yang, D.S. (2011). Autophagy failure in Alzheimer's disease--locating the primary defect. Neurobiology of disease *43*, 38-45. 10.1016/j.nbd.2011.01.021.
Nixon, R.A., and Yang, D.S. (2012). Autophagy and neuronal cell death in neurological disorders. Cold Spring Harbor perspectives in biology *4*. 10.1101/cshperspect.a008839.
Nixon, R.A., Yang, D.S., and Lee, J.H. (2008). Neurodegenerative lysosomal disorders: a continuum from development to late age. Autophagy *4*, 590-599. 10.4161/auto.6259.
Nygaard, H.B., van Dyck, C.H., and Strittmatter, S.M. (2014). Fyn kinase inhibition as a novel therapy for Alzheimer's disease. Alzheimer's research & therapy *6*, 8. 10.1186/alzrt238.
Oakley, H., Cole, S.L., Logan, S., Maus, E., Shao, P., Craft, J., Guillozet-Bongaarts, A., Ohno, M., Disterhoft, J., Van Eldik, L., et al. (2006). Intraneuronal beta-amyloid aggregates, neurodegeneration, and neuron loss in transgenic mice with five familial Alzheimer's disease mutations: potential factors in amyloid plaque formation. J Neurosci *26*, 10129-10140. 10.1523/jneurosci.1202-06.2006.
Pera, M., Alcolea, D., Sanchez-Valle, R., Guardia-Laguarta, C., Colom-Cadena, M., Badiola, N., Suarez-Calvet, M., Llado, A., Barrera-Ocampo, A.A., Sepulveda-Falla, D., et al. (2013). Distinct patterns of APP processing in the CNS in autosomal-dominant and sporadic Alzheimer disease. Acta Neuropathol *125*, 201-213. 10.1007/s00401-012-1062-9.
Perluigi, M., and Butterfield, D.A. (2012). Oxidative Stress and Down Syndrome: A Route toward Alzheimer-Like Dementia. Curr Gerontol Geriatr Res *2012*, 724904. 10.1155/2012/724904.
Pitsi, D., and Octave, J.N. (2004). Presenilin 1 stabilizes the C-terminal fragment of the amyloid precursor protein independently of gamma-secretase activity. J Biol Chem *279*, 25333-25338. 10.1074/jbc.M312710200.
Poulsen, E.T., Iannuzzi, F., Rasmussen, H.F., Maier, T.J., Enghild, J.J., Jorgensen, A.L., and Matrone, C. (2017). An Aberrant Phosphorylation of Amyloid Precursor Protein Tyrosine Regulates Its Trafficking and the Binding to the Clathrin Endocytic Complex in Neural Stem Cells of Alzheimer's Disease Patients. Front Mol Neurosci *10*, 59. 10.3389/fnmol.2017.00059.
Radzimanowski, J., Simon, B., Sattler, M., Beyreuther, K., Sinning, I., and Wild, K. (2008). Structure of the intracellular domain of the amyloid precursor protein in complex with Fe65-PTB2. EMBO Rep *9*, 1134-1140. 10.1038/embor.2008.188.
Rappsilber, J., Mann, M., and Ishihama, Y. (2007). Protocol for micro-purification, enrichment, pre-fractionation and storage of peptides for proteomics using StageTips. Nat Protoc *2*, 1896-1906. 10.1038/nprot.2007.261.
Russo, C., Salis, S., Dolcini, V., Venezia, V., Song, X.H., Teller, J.K., and Schettini, G. (2001). Amino-terminal modification and tyrosine phosphorylation of [corrected] carboxy-terminal fragments of the amyloid precursor protein in Alzheimer's disease and Down's syndrome brain. Neurobiology of disease *8*, 173-180. 10.1006/nbdi.2000.0357.
Salehi, A., Delcroix, J.D., Belichenko, P.V., Zhan, K., Wu, C., Valletta, J.S., Takimoto-Kimura, R., Kleschevnikov, A.M., Sambamurti, K., Chung, P.P., et al. (2006). Increased App expression in a mouse model of Down's syndrome disrupts NGF transport and causes cholinergic neuron degeneration. Neuron *51*, 29-42. 10.1016/j.neuron.2006.05.022.
Shen, R., Zhao, X., He, L., Ding, Y., Xu, W., Lin, S., Fang, S., Yang, W., Sung, K., Spencer, B., et al. (2020). Upregulation of RIN3 induces endosomal dysfunction in Alzheimer's disease. Transl Neurodegener *9*, 26. 10.1186/s40035-020-00206-1.
Shirazi, S.K., and Wood, J.G. (1993). The protein tyrosine kinase, fyn, in Alzheimer's disease pathology. Neuroreport *4*, 435-437. 10.1097/00001756-199304000-00024.

Stransky, L.A., and Forgac, M. (2015). Amino Acid Availability Modulates Vacuolar H+-ATPase Assembly. J Biol Chem *290*, 27360-27369. 10.1074/jbc.M115.659128.
Tam, J.H., Cobb, M.R., Seah, C., and Pasternak, S.H. (2016). Tyrosine Binding Protein Sites Regulate the Intracellular Trafficking and Processing of Amyloid Precursor Protein through a Novel Lysosome-Directed Pathway. PLoS One *11*, e0161445. 10.1371/journal.pone.0161445.
Tamayev, R., Matsuda, S., Arancio, O., and D'Adamio, L. (2012). β- but not γ-secretase proteolysis of APP causes synaptic and memory deficits in a mouse model of dementia. EMBO molecular medicine *4*, 171-179. 10.1002/emmm.201100195.
Tarr, P.E., Contursi, C., Roncarati, R., Noviello, C., Ghersi, E., Scheinfeld, M.H., Zambrano, N., Russo, T., and D'Adamio, L. (2002). Evidence for a role of the nerve growth factor receptor TrkA in tyrosine phosphorylation and processing of beta-APP. Biochem Biophys Res Commun *295*, 324-329. 10.1016/s0006-291x(02)00678-2.
Tian, Y., Chang, J.C., Greengard, P., and Flajolet, M. (2014). The convergence of endosomal and autophagosomal pathways: implications for APP-CTF degradation. Autophagy *10*, 694-696. 10.4161/auto.27802.
Tsui, V., and Case, D.A. (2000). Theory and applications of the generalized Born solvation model in macromolecular simulations. Biopolymers *56*, 275-291. 10.1002/1097-0282(2000)56:4<275::Aid-bip10024>3.0.Co;2-e.
Villar, A.J., Belichenko, P.V., Gillespie, A.M., Kozy, H.M., Mobley, W.C., and Epstein, C.J. (2005). Identification and characterization of a new Down syndrome model, Ts[Rb(12.1716)]2Cje, resulting from a spontaneous Robertsonian fusion between T(171)65Dn and mouse chromosome 12. Mammalian genome : official journal of the International Mammalian Genome Society *16*, 79-90. 10.1007/s00335-004-2428-7.
Walker, M.W., and Lloyd-Evans, E. (2015). A rapid method for the preparation of ultrapure, functional lysosomes using functionalized superparamagnetic iron oxide nanoparticles. Methods Cell Biol *126*, 21-43. 10.1016/bs.mcb.2014.10.019.
Wang, Y., Martinez-Vicente, M., Kruger, U., Kaushik, S., Wong, E., Mandelkow, E.M., Cuervo, A.M., and Mandelkow, E. (2009). Tau fragmentation, aggregation and clearance: the dual role of lysosomal processing. Hum Mol Genet *18*, 4153-4170. 10.1093/hmg/ddp367.
Wang, Z., Zhang, Q., Lin, J.R., Jabalameli, M.R., Mitra, J., Nguyen, N., and Zhang, Z.D. (2021). Deep post-GWAS analysis identifies potential risk genes and risk variants for Alzheimer's disease, providing new insights into its disease mechanisms. Scientific reports *11*, 20511. 10.1038/s41598-021-99352-3.
Wolfe, D.M., Lee, J.H., Kumar, A., Lee, S., Orenstein, S.J., and Nixon, R.A. (2013). Autophagy failure in Alzheimer's disease and the role of defective lysosomal acidification. Eur J Neurosci *37*, 1949-1961. 10.1111/ejn.12169.
Woodruff, G., Reyna, S.M., Dunlap, M., Van Der Kant, R., Callender, J.A., Young, J.E., Roberts, E.A., and Goldstein, L.S. (2016). Defective Transcytosis of APP and Lipoproteins in Human iPSC-Derived Neurons with Familial Alzheimer's Disease Mutations. Cell Rep *17*, 759-773. 10.1016/j.celrep.2016.09.034.
Yáñez, M.J., Belbin, O., Estrada, L.D., Leal, N., Contreras, P.S., Lleó, A., Burgos, P.V., Zanlungo, S., and Alvarez, A.R. (2016). c-Abl links APP-BACE1 interaction promoting APP amyloidogenic processing in Niemann-Pick type C disease. Biochimica et biophysica acta *1862*, 2158-2167. 10.1016/j.bbadis.2016.08.016.

Yang, L.B., Lindholm, K., Yan, R., Citron, M., Xia, W., Yang, X.L., Beach, T., Sue, L., Wong, P., Price, D., et al. (2003). Elevated beta-secretase expression and enzymatic activity detected in sporadic Alzheimer disease. Nat Med *9*, 3-4. 10.1038/nm0103-3.
Zambrano, N., Bruni, P., Minopoli, G., Mosca, R., Molino, D., Russo, C., Schettini, G., Sudol, M., and Russo, T. (2001). The beta-amyloid precursor protein APP is tyrosine-phosphorylated in cells expressing a constitutively active form of the Abl protoncogene. J Biol Chem *276*, 19787-19792. 10.1074/jbc.M100792200.
Zoncu, R., Bar-Peled, L., Efeyan, A., Wang, S., Sancak, Y., and Sabatini, D.M. (2011). mTORC1 senses lysosomal amino acids through an inside-out mechanism that requires the vacuolar H(+)-ATPase. Science *334*, 678-683. 10.1126/science.1207056.
Zuliani, G., Trentini, A., Rosta, V., Guerrini, R., Pacifico, S., Bonazzi, S., Guiotto, A., Passaro, A., Seripa, D., Valacchi, G., and Cervellati, C. (2020). Increased blood BACE1 activity as a potential common pathogenic factor of vascular dementia and late onset Alzheimer's disease. Scientific reports *10*, 14980. 10.1038/s41598-020-72168-3.

Figure 1

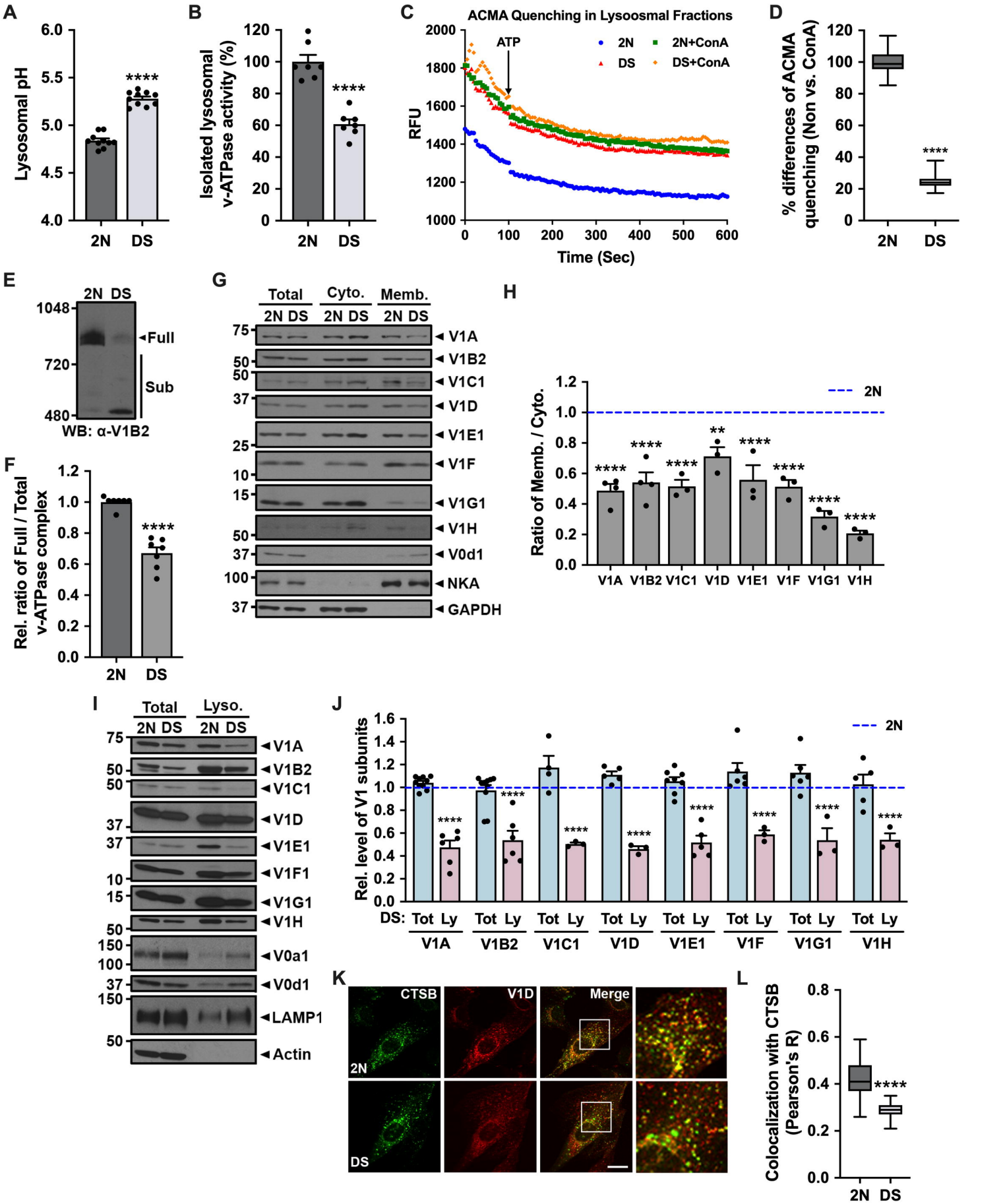
A
Lysosomal pH
6.0
5.5
5.0
4.5
4.0
****
2N
DS
B
Isolated lysosomal v-ATPase activity (%)
120
100
80
60
40
20
0
****
2N
DS
C
ACMA Quenching in Lysoosmal Fractions
ATP
2N
2N+ConA
DS
DS+ConA
RFU
2000
1800
1600
1400
1200
1000
0
100
200
300
400
500
600
Time (Sec)
D
% differences of ACMA quenching (Non vs. ConA)
120
100
80
60
40
20
0
****
2N
DS
E
2N DS
1048
720
480
Full
Sub
WB: α-V1B2
F
Rel. ratio of Full / Total v-ATPase complex
1.2
1.0
0.8
0.6
0.4
0.2
0.0
****
2N
DS
G
Total
Cyto.
Memb.
2N DS
2N DS
2N DS
75
50
50
37
25
10
15
50
37
100
37
V1A
V1B2
V1C1
V1D
V1E1
V1F
V1G1
V1H
V0d1
NKA
GAPDH
H
Ratio of Memb. / Cyto.
1.2
1.0
0.8
0.6
0.4
0.2
0.0
2N
****
****
****
**
****
****
****
****
V1A
V1B2
V1C1
V1D
V1E1
V1F
V1G1
V1H
I
Total
Lyso.
2N DS
2N DS
75
50
50
37
37
10
15
50
150
100
37
150
50
V1A
V1B2
V1C1
V1D
V1E1
V1F1
V1G1
V1H
V0a1
V0d1
LAMP1
Actin
J
Rel. level of V1 subunits
1.6
1.4
1.2
1.0
0.8
0.6
0.4
0.2
0.0
2N
****
DS:
Tot Ly
V1A
V1B2
V1C1
V1D
V1E1
V1F
V1G1
V1H
K
CTSB
V1D
Merge
2N
DS
L
Colocalization with CTSB (Pearson's R)
0.8
0.6
0.4
0.2
0.0
****
2N
DS

Figure 2

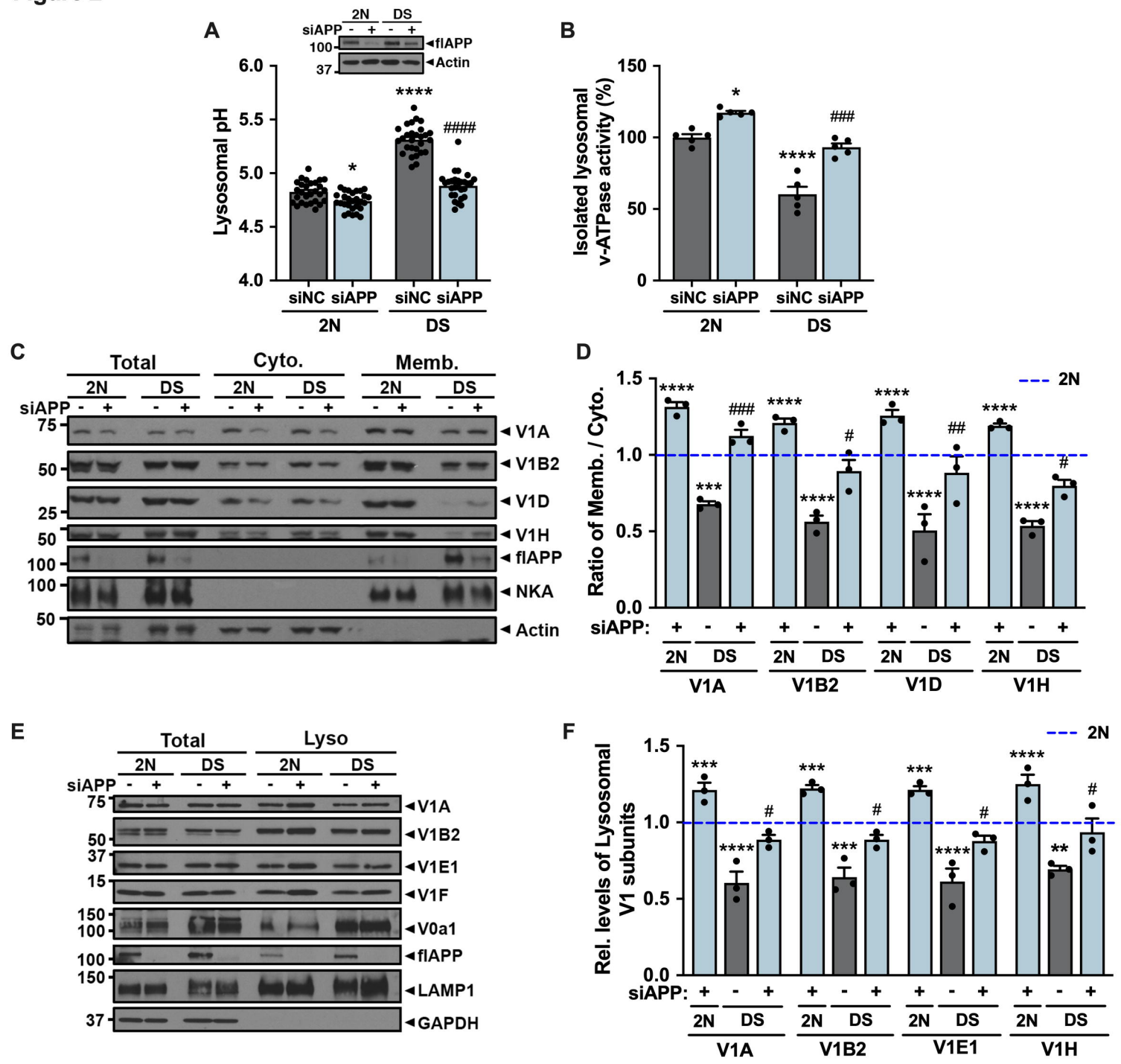
A
2N
DS
siAPP
flAPP
Actin
Lysosomal pH
siNC
siAPP
2N
DS
B
Isolated lysosomal v-ATPase activity (%)
C
Total
Cyto.
Memb.
V1A
V1B2
V1D
V1H
flAPP
NKA
Actin
D
Ratio of Memb. / Cyto.
siAPP:
V1A
V1B2
V1D
V1H
E
Lyso
V1E1
V0a1
LAMP1
GAPDH
F
Rel. levels of Lysosomal V1 subunits

Figure 3

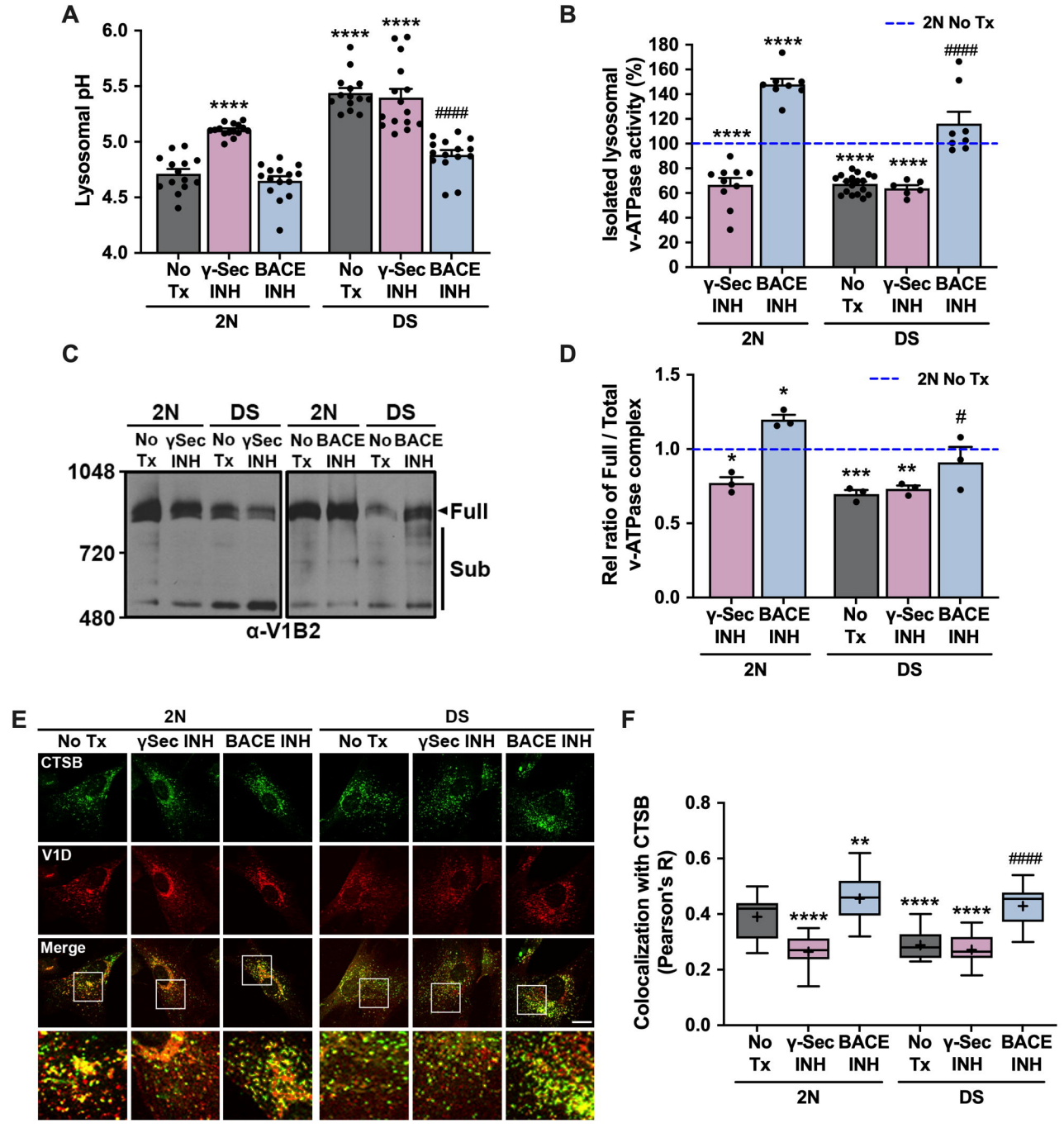
A
Lysosomal pH
6.0
5.5
5.0
4.5
4.0
****
****
****
####
No Tx
γ-Sec INH
BACE INH
No Tx
γ-Sec INH
BACE INH
2N
DS
B
2N No Tx
Isolated lysosomal v-ATPase activity (%)
180
160
140
120
100
80
60
40
20
0
****
****
****
****
####
γ-Sec INH
BACE INH
No Tx
γ-Sec INH
BACE INH
2N
DS
C
2N
DS
2N
DS
No Tx
γSec INH
No Tx
γSec INH
No Tx
BACE INH
No Tx
BACE INH
1048
720
480
Full
Sub
α-V1B2
D
2N No Tx
Rel ratio of Full / Total v-ATPase complex
1.5
1.0
0.5
0.0
*
*
***
**
#
γ-Sec INH
BACE INH
No Tx
γ-Sec INH
BACE INH
2N
DS
E
2N
DS
No Tx
γSec INH
BACE INH
No Tx
γSec INH
BACE INH
CTSB
V1D
Merge
F
Colocalization with CTSB (Pearson's R)
0.8
0.6
0.4
0.2
0.0
**
****
****
****
####
No Tx
γ-Sec INH
BACE INH
No Tx
γ-Sec INH
BACE INH
2N
DS

Figure 4

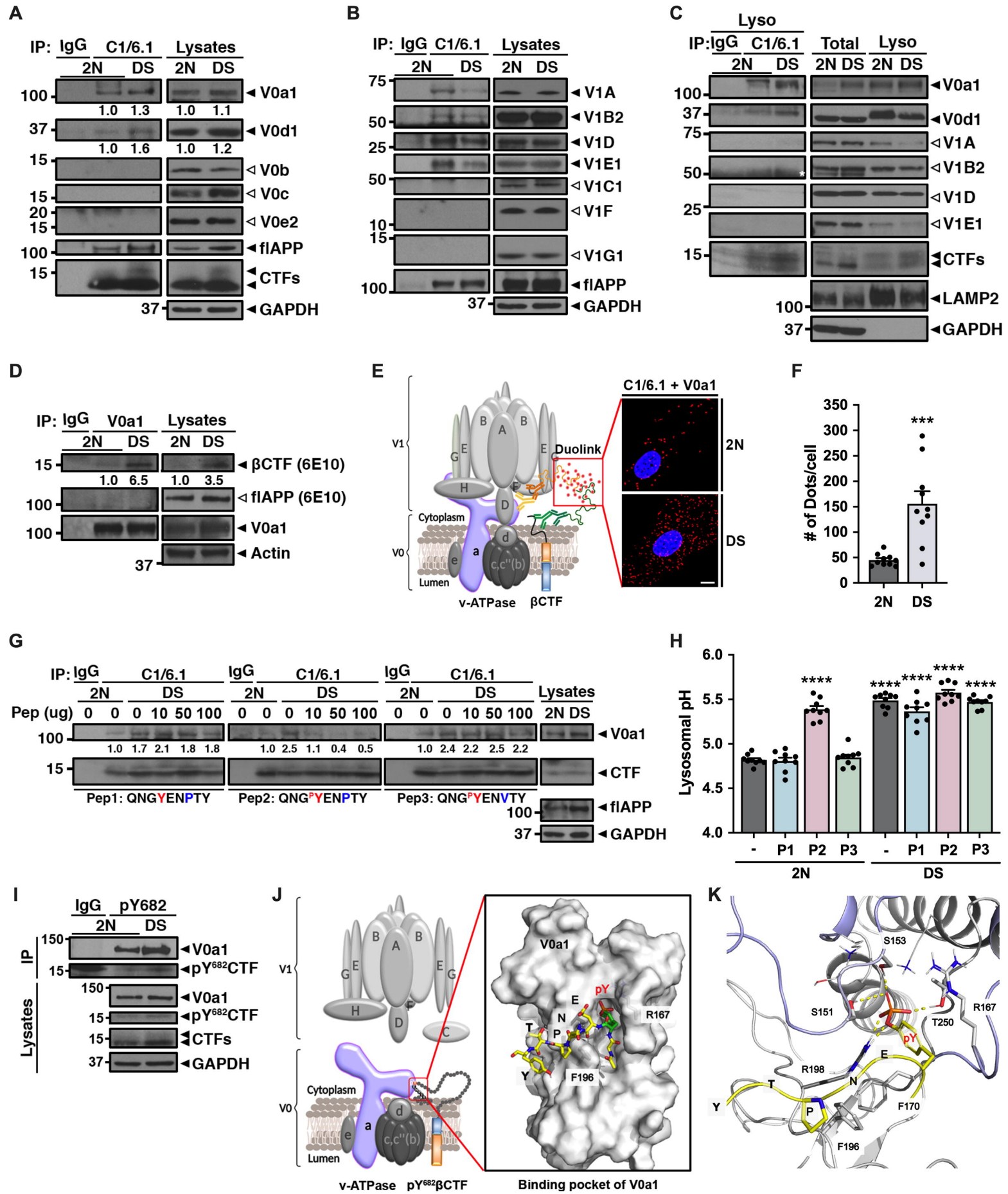
A
IP: IgG C1/6.1 Lysates
2N DS 2N DS
100 V0a1
1.0 1.3 1.0 1.1
37 V0d1
1.0 1.6 1.0 1.2
15 V0b
15 V0c
20 15 V0e2
100 flAPP
15 CTFs
37 GAPDH
B
IP: IgG C1/6.1 Lysates
2N DS 2N DS
75 V1A
50 V1B2
25 V1D
V1E1
50 V1C1
10 V1F
15 V1G1
100 flAPP
37 GAPDH
C
Lyso
IP: IgG C1/6.1 Total Lyso
2N DS 2N DS 2N DS
100 V0a1
37 V0d1
75 V1A
50 V1B2
25 V1D
V1E1
15 CTFs
100 LAMP2
37 GAPDH
D
IP: IgG V0a1 Lysates
2N DS 2N DS
15 βCTF (6E10)
1.0 6.5 1.0 3.5
100 flAPP (6E10)
100 V0a1
37 Actin
E
V1
V0
Cytoplasm
Lumen
Duolink
v-ATPase βCTF
C1/6.1 + V0a1
2N
DS
F
350 300 250 200 150 100 50 0
# of Dots/cell
***
2N DS
G
IP: IgG C1/6.1 IgG C1/6.1 IgG C1/6.1 Lysates
2N DS 2N DS 2N DS 2N DS
Pep (ug) 0 0 0 10 50 100 0 0 0 10 50 100 0 0 0 10 50 100
100 V0a1
1.0 1.7 2.1 1.8 1.8 1.0 2.5 1.1 0.4 0.5 1.0 2.4 2.2 2.5 2.2
15 CTF
Pep1: QNGYENPTY Pep2: QNGPYENPTY Pep3: QNGPYENVTY
100 flAPP
37 GAPDH
H
6.0 5.5 5.0 4.5 4.0
Lysosomal pH
****
- P1 P2 P3 - P1 P2 P3
2N DS
I
IgG pY682
2N DS
IP
150 V0a1
15 pY682CTF
Lysates
150 V0a1
15 pY682CTF
15 CTFs
37 GAPDH
J
V1
V0
Cytoplasm
Lumen
v-ATPase pY682βCTF
V0a1
pY
E
N
T
P
Y
R167
F196
Binding pocket of V0a1
K
S153
S151
R167
T250
pY
E
R198
N
T
Y
P
F170
F196

Figure 5

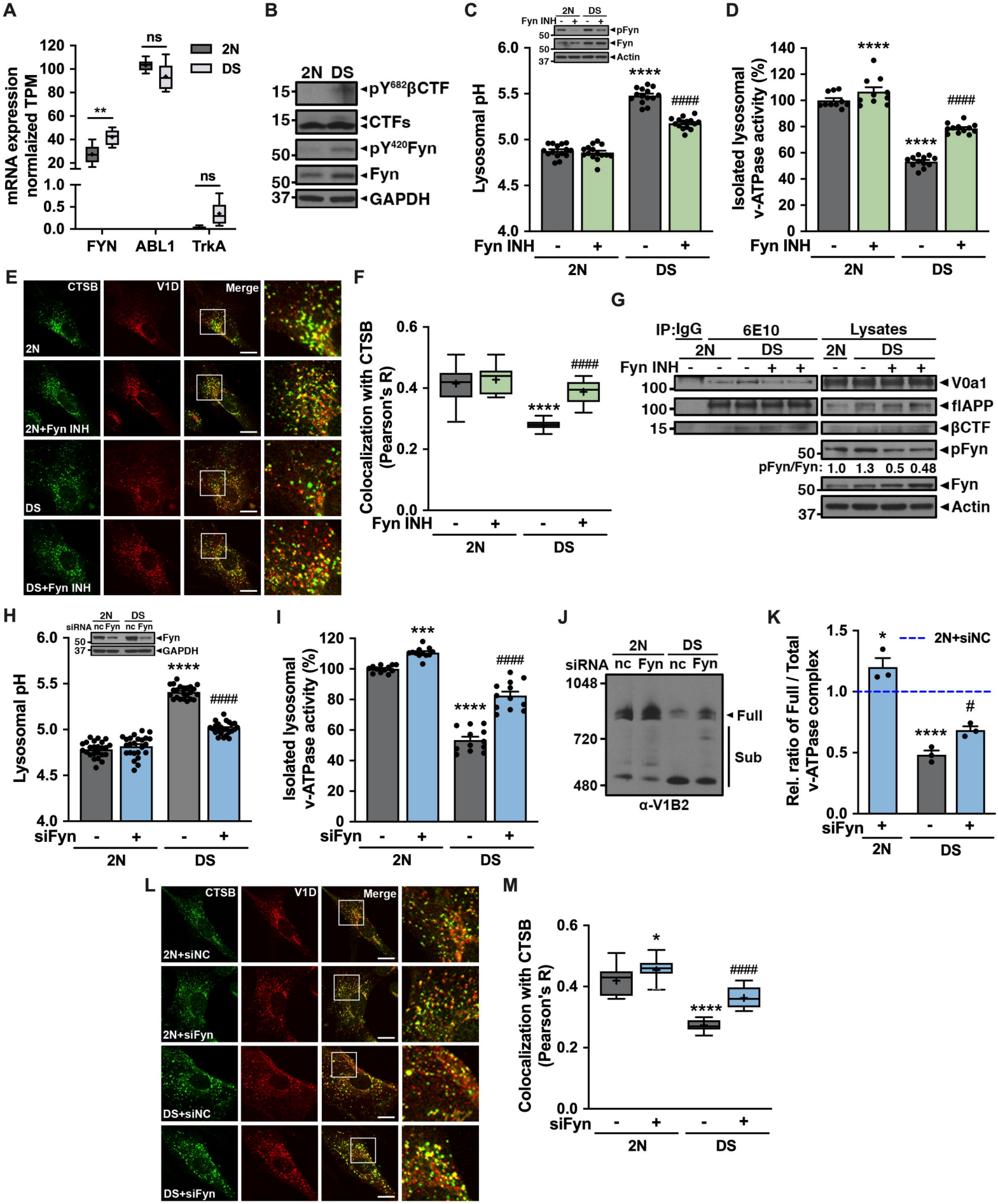
A
mRNA expression normlaized TPM
2N
DS
ns
**
ns
FYN
ABL1
TrkA
B
2N DS
pY682βCTF
CTFs
pY420Fyn
Fyn
GAPDH
C
Lysosomal pH
Fyn INH
pFyn
Fyn
Actin
****
####
2N
DS
D
Isolated lysosomal v-ATPase activity (%)
Fyn INH
E
CTSB
V1D
Merge
2N
2N+Fyn INH
DS
DS+Fyn INH
F
Colocalization with CTSB (Pearson's R)
Fyn INH
G
IP:IgG
6E10
Lysates
V0a1
flAPP
βCTF
pFyn
pFyn/Fyn: 1.0 1.3 0.5 0.48
Fyn
Actin
H
siRNA nc Fyn nc Fyn
Lysosomal pH
siFyn
I
Isolated lysosomal v-ATPase activity (%)
***
J
siRNA nc Fyn nc Fyn
Full
Sub
α-V1B2
K
Rel. ratio of Full / Total v-ATPase complex
2N+siNC
L
2N+siNC
2N+siFyn
DS+siNC
DS+siFyn
M
Colocalization with CTSB (Pearson's R)
siFyn

Figure 6

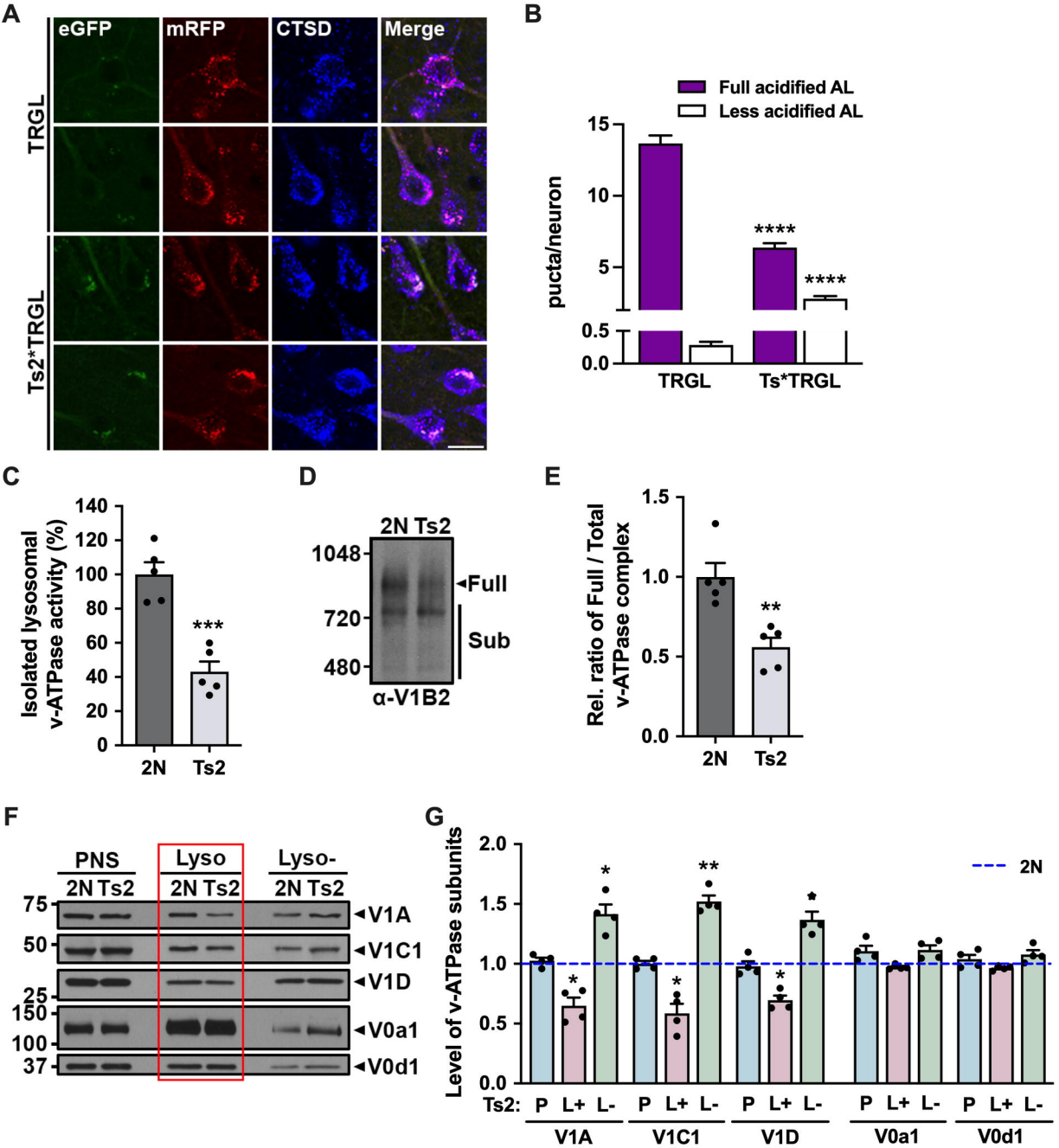
A
eGFP
mRFP
CTSD
Merge
TRGL
Ts2*TRGL
B
Full acidified AL
Less acidified AL
pucta/neuron
15
10
5
0.5
0.0
****
****
TRGL
Ts*TRGL
C
Isolated lysosomal v-ATPase activity (%)
140
120
100
80
60
40
20
0
***
2N
Ts2
D
2N Ts2
1048
720
480
Full
Sub
α-V1B2
E
Rel. ratio of Full / Total v-ATPase complex
1.5
1.0
0.5
0.0
**
2N
Ts2
F
PNS
Lyso
Lyso-
2N Ts2
2N Ts2
2N Ts2
75
50
25
150
100
37
V1A
V1C1
V1D
V0a1
V0d1
G
Level of v-ATPase subunits
2.0
1.5
1.0
0.5
0.0
2N
Ts2:
P
L+
L-
V1A
V1C1
V1D
V0a1
V0d1

Figure 7

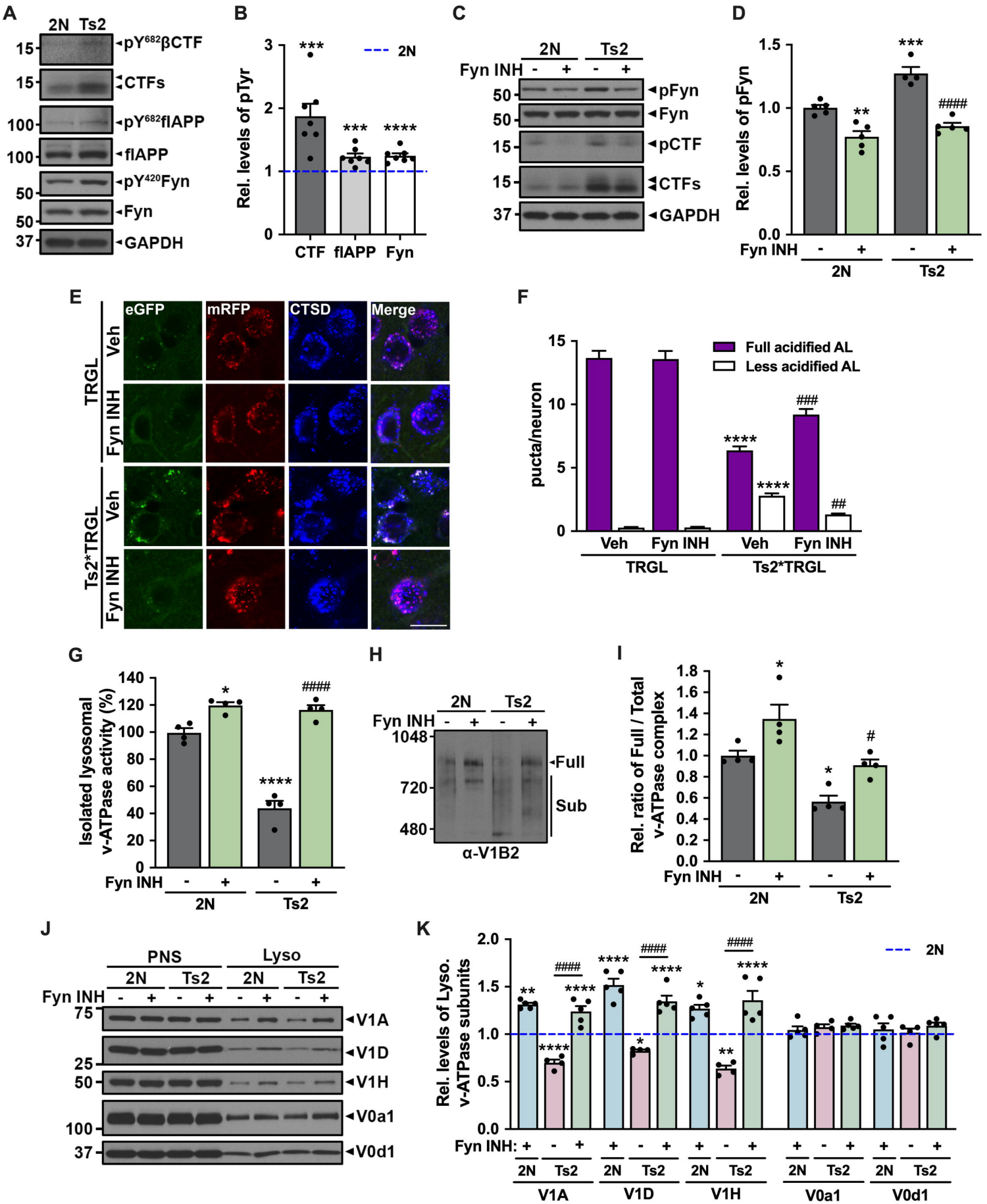
A
2N Ts2
15
15
100
100
50
50
37
pY682βCTF
CTFs
pY682flAPP
flAPP
pY420Fyn
Fyn
GAPDH
B
Rel. levels of pTyr
2N
CTF flAPP Fyn
C
2N Ts2
Fyn INH - + - +
50 pFyn
50 Fyn
15 pCTF
15 CTFs
37 GAPDH
D
Rel. levels of pFyn
Fyn INH - + - +
2N Ts2
E
eGFP mRFP CTSD Merge
TRGL Veh
TRGL Fyn INH
Ts2*TRGL Veh
Ts2*TRGL Fyn INH
F
pucta/neuron
Full acidified AL
Less acidified AL
Veh Fyn INH Veh Fyn INH
TRGL Ts2*TRGL
G
Isolated lysosomal v-ATPase activity (%)
Fyn INH - + - +
2N Ts2
H
2N Ts2
Fyn INH - + - +
1048
720
480
Full
Sub
α-V1B2
I
Rel. ratio of Full / Total v-ATPase complex
Fyn INH - + - +
2N Ts2
J
PNS Lyso
2N Ts2 2N Ts2
Fyn INH - + - + - + - +
75 V1A
25 V1D
50 V1H
100 V0a1
37 V0d1
K
Rel. levels of Lyso. v-ATPase subunits
2N
Fyn INH: + - + + - + + - + + - + + - +
2N Ts2 2N Ts2 2N Ts2 2N Ts2 2N Ts2
V1A V1D V1H V0a1 V0d1